INTERNATIONAL JOURNAL FOR NUMERICAL METHODS IN FLUIDS VOL. 21, 49–74 (1995)

CALCULATION OF REYNOLDS STRESSES IN TURBULENT SUPERSONIC FLOWS

FOLUSO LADEINDE AND JOHN C. INTILE

Mechanical Engineering Department, SUNY at Stony Brook, Stony Brook, NY 11794-2300, U.S.A.

SUMMARY

The baseline numerical procedure of interest in this study combines flux vector splitting, flux difference splitting and an explicit treatment of the diffusion terms of the flow equations. The viscous terms are treated explicitly to preserve the wave propagation properties of the Euler fluxes and permit splitting. The experience with this scheme has been limited to laminar or, at best, 'eddy viscosity' flows. In this paper the applicability of the scheme is extended to include the calculation of turbulent Reynolds stresses in supersonic flows. The schemes and our implementation are discussed. Both laminar and turbulence subsets of the Reynolds/Favre-averaged equations are tested, with a discussion of relative performance. The test problem for turbulence consists of a zero-pressure-gradient supersonic boundary layer as well as a supersonic boundary layer experiencing the combined effects of adverse pressure gradient, bulk compression and a concave streamline curvature. Excellent agreement with experimental measurements is observed for most of the quantities compared, which suggests that the numerical procedures presented in this paper are potentially very useful.

KEY WORDS flux splitting; Reynolds stresses; finite volume; turbulence

1. INTRODUCTION

Our studies have the ultimate goal of producing a programme which can be used to generate reliable engineering design data for realistic aerodynamic (supersonic and hypersonic) systems. We also want numerical calculations that could be used for some fundamental studies of turbulence.

Most engineering fluid dynamic problems involve turbulent flows and it seems that modelling of the turbulence is a feasible way to attack the analysis. However, in the hierarchy of turbulence models it appears that the simplest models that have any chance of dealing with realistic engineering problems are those based on second-moment closures.[1] Lower-order models have serious defects that preclude them from consideration for all but the simplest systems. For instance, zero-equation models such as the Baldwin–Lomax[2] model are seriously limited by the near-wall formulation, while two-equation models such as k–ε or k–ω are based on assumptions which, among other things, prevent accurate simulation of flows with significant normal stresses.[3] Second-moment calculations can provide engineering design data as well as data that could be used for more fundamental studies of some aspects of turbulence.

It is well known that turbulence models, including those based on second-moment closures, have not always performed well. Another complicating factor is the choice of numerical method, for which there are multitudes of options with varying degrees of efficiency. In the rest of this section we will discuss some of these schemes, pointing out their strengths and weaknesses. We will conclude the section with a discussion of the baseline scheme upon which our work is based.

CCC 0271–2091/95/010049–26

Received 24 February 1994
Revised 4 October 1994

Options for calculating the equations of interest in this work include the flux-difference-splitting (FDS) schemes such as those of Roe,[4] Harten and Lax[5] and Rusanov,[6] the flux-vector-splitting (FVS) schemes[7,8] as well as central difference schemes.[9,10] Of these, Roe's method has been shown to be the most accurate and the one that gives the sharpest shock resolution.[11] From the comparison exercise,[11] one-fifth to one-half as many points were required to resolve a shear layer using Roe's fluxes in a first-order scheme compared with using other fluxes in second- or even third-order schemes. This would seem to be quite important especially in three-dimensional flows, where a large pay-off might be gained by the use of fewer points. However, all three schemes have defects. The basic Roe scheme could produce entropy-violating solutions[12] and has a slower convergence compared with FVS.[13] FVS tends to be too diffusive,[13] while the central difference schemes usually involve the explicit addition of dissipation,[9,10] with the attendant issue of 'how much is enough at a location'. Further, in current implementation none of the procedures performs well when shocks are not aligned normally to cell surfaces.[14]

Another potential candidate for use with high-speed flow simulation is the Gauss–Seidel method of MacCormack.[15] This is a line method with a Gauss–Seidel treatment of 'out-of-line' terms. When applied to the two-dimensional Navier–Stokes equations for steady state transonic cascade flow, very impressive performance was reported:[15] 50 time steps to reach convergence, with CFL values as high as 10^8. Unfortunately, extension of the cascade problem to three dimensions met with severe numerical convergence difficulties.[15] Moreover, MacCormack[15] observed that a three-dimensional algorithm that worked (for the cascade problem) is approximately twice as expensive as an approximate factorization scheme and it is not clear that this algorithm will work for general three-dimensional flows.

Other options of numerical methods include the diagonalized alternating direction implicit methods, with and without approximate factorization or multigrid[16–18], and the diagonally inverted LU implicit multigrid scheme.[19–23] In one implementation of this approach the time-linearized implicit operator is approximated as the product of three one-dimensional factors, each of which is diagonalized by a local similarity transformation. Thus only a decoupled system of scalar pentadiagonal equations need be solved along each line. This approach is believed to have good high-wave-number damping, making it a suitable algorithm for smoothening in multigrid approaches. Yokota[20] has applied this method to solve the Reynolds-averaged equations using the k–ε method. The method appears promising. In fact, the k–ε equations involve a simple 2×2 matrix system which can be inverted algebraically using the similarity transformation approach. However, in our opinion one disadvantage of this approach relative to flux splitting (Roe or Steger–Warming) is the explicit addition of dissipation terms. A blend is used: fourth-difference terms to prevent odd–even decoupling and second-difference terms to stabilize the calculations near shocks. A procedure to determine the optimum amount of dissipation for a variety of situations would be desirable.

HOPE and AUSM[24] are two new options of numerical methods, of which AUSM is more promising from the standpoint of non-entropy violation, accuracy, computational efficiency, simplicity and the ability to give good results when shocks are not aligned normally to cell surfaces. From their studies, Liou and Steffen[24] seem to have understood the cause of the diffusion error that is present in van Leer's method as well as the non-physical entropy-violating solutions that have been observed with the basic Roe method. Using a splitting of the advective velocity component, AUSM is formulated to take care of these problems, giving high accuracy with reduced complexity and computational effort and an efficiency that rivals FVS. As an example, AUSM does not exhibit the so-called carbuncle phenomenon that has been observed when e.g. the basic Roe scheme is used to calculate supersonic flows over circular cylinders.[12] However, AUSM is not yet well established.

For very-high-order calculations the essentially non-oscillatory (ENO) schemes[25] come to mind. These are extensions of the Godunov scheme in which high accuracy is obtained by using a large stencil and a 'reconstruction' process that employs cell-averaged values in the stencil. Discretization

across discontinuities (and hence the Gibbs phenomenon) is inhibited by choosing the stencil adaptively from the smooth part of the flow. There are several variations of the ENO procedure, one of which works directly on the fluxes rather than the cell averages and uses a special class of TVD high-order Runge–Kutta scheme for time integration.[26] The high accuracy of ENO scheme makes them of interest in direct numerical simulation (DNS) of turbulence, where comparisons with the traditional spectral method have shown excellent agreement.[26] The so-called compact (Padé approximant) procedures are also useful in this regard.[27] However, the ENO and compact schemes tend to be very expensive.

For the present studies we are interested in an implicit, finite volume, LU procedure in which FVS and FDS are combined[13] to utilize the best of these two common methods: faster convergence in the case of FVS and more accurate results and sharp resolution of shocks in the case of FDS. Calculations based on this scheme have been observed to give good performance on a variety of high-speed flows.[13,28] However, the experience with this scheme has been limited to laminar or eddy viscosity flows. The contribution of the present work can be found in the extension of the approach to include the transport equations for the six components of the Reynolds stress tensor and an additional equation for turbulence dissipation. In the following section the mean equations are given. This is followed by a discussion of the closure models and the final form of the turbulence equations. We then present the numerical procedure and our implementation. Sample results are given for the shock tube problem and Carter's supersonic laminar boundary layer problem. We also calculated a zero-pressure-gradient supersonic turbulent boundary layer (TBL) as well as a TBL experiencing the combined effects of an adverse pressure gradient, bulk compression and concave surface curvature. Excellent results were observed compared with experimental measurements.

2. GOVERNING EQUATIONS

To obtain the mean flow equations, the Navier–Stokes equations are first Reynolds averaged. We then apply Favre (mass) averaging in order to get the equations in a relatively simple form. The resulting equations are shown below, where an 'overbar' indicates the mean relative to Reynolds averaging, with a 'double prime' indicating the fluctuation. A 'tilde' and a 'single prime' are the corresponding notations for Favre averaging.

Conservation of mass:

$$\frac{\partial \bar{\rho}}{\partial t} + \frac{\partial(\bar{\rho}\tilde{u}_k)}{\partial x_k} = 0. \tag{1}$$

Conservation of momentum:

$$\frac{\partial(\bar{\rho}\tilde{u}_i)}{\partial t} + \frac{\partial(\bar{\rho}\tilde{u}_i\tilde{u}_k)}{\partial x_k} = -\frac{\partial \bar{\phi}}{\partial x_i} + \frac{\partial \bar{\sigma}_{ik}}{\partial x_k} + \frac{\partial \tau_{ik}}{\partial x_k}, \tag{2}$$

where the Favre-averaged Reynolds stress tensor is

$$\tau_{ij} = -\bar{\rho}\widetilde{u_i'u_j'}. \tag{3}$$

Conservation of energy:

$$\frac{\partial(\bar{\rho}\tilde{E})}{\partial t} + \frac{\partial}{\partial x_k}[\tilde{u}_k(\bar{\rho}\tilde{E} + \bar{p})] = \frac{\partial}{\partial x_k}(\bar{\sigma}_{jk}\tilde{u}_j - \bar{q}_k) + \frac{\partial}{\partial x_k}(\widetilde{\sigma_{jk}''u_j''} - \overline{p''u_k''} - \bar{\rho}\widetilde{E'u_k'}). \tag{4}$$

The turbulent energy flux $\widetilde{E'u_k'}$ is defined to be

$$\widetilde{E'u_k'} = C_v\widetilde{T'u_k'} + \tilde{u}_j\widetilde{u_k'u_j'} + \frac{\widetilde{u_j'u_j'u_k'}}{2}. \tag{5}$$

The mean viscous stress tensor $\bar{\sigma}_{ij}$ is given by

$$\bar{\sigma}_{ij} = \overline{\mu\left(\frac{\partial u_i}{\partial x_j} + \frac{\partial u_j}{\partial x_i}\right)} - \frac{2}{3}\overline{\mu\frac{\partial u_k}{\partial x_k}}\delta_{ij} \approx \bar{\mu}\left(\frac{\partial \tilde{u}_i}{\partial x_j} + \frac{\partial \tilde{u}_j}{\partial x_i}\right) - \frac{2}{3}\bar{\mu}\frac{\partial \tilde{u}_k}{\partial x_k}\delta_{ij}, \tag{6}$$

while the mean heat flux is approximated as

$$\bar{q}_k = -\overline{\kappa\frac{\partial T}{\partial x_k}} \approx -\bar{\kappa}\frac{\partial \tilde{T}}{\partial x_k}. \tag{7}$$

The mean pressure is related to the mean density and temperature through the equation of state

$$\bar{p} = \bar{\rho}R\tilde{T} \tag{8}$$

and thus

$$\bar{p} = (\gamma - 1)(\bar{\rho}\tilde{E} - \tfrac{1}{2}\bar{\rho}\tilde{u}_i\tilde{u}_i - \tfrac{1}{2}\widetilde{\bar{\rho}u_i'u_i'}) = (\gamma - 1)\bar{\rho}\tilde{e}. \tag{9}$$

In these equations $\rho, t, x_i, u_i, p, T, E, q, C_v, \mu, \kappa, R, e$ and γ denote density, time, ith co-ordinate direction, ith velocity component, pressure, temperature, total energy, heat flux, specific heat at constant volume, absolute viscosity, thermal conductivity, gas constant, internal energy and ratio of specific heat respectively.

The mean equations can be written in a more compact form for clarity:

$$\frac{\partial \mathbf{q}}{\partial t} + \frac{\partial \mathbf{G}^k}{\partial x_k} = \frac{\partial \mathbf{G}_v^k}{\partial x_k}, \tag{10}$$

where

$$\mathbf{q} = \begin{bmatrix} \bar{\rho} \\ \bar{\rho}\tilde{u}_1 \\ \bar{\rho}\tilde{u}_2 \\ \bar{\rho}\tilde{u}_3 \\ \bar{\rho}\tilde{E} \end{bmatrix} \tag{11}$$

is the vector of conserved variables,

$$\mathbf{G}^k \equiv \begin{bmatrix} \mathbf{G}^1 & \mathbf{G}^2 & \mathbf{G}^3 \end{bmatrix} = \begin{bmatrix} \bar{\rho}\tilde{u}_1 & \bar{\rho}\tilde{u}_2 & \bar{\rho}\tilde{u}_3 \\ \bar{\rho}\tilde{u}_1\tilde{u}_1 + \bar{p} & \bar{\rho}\tilde{u}_1\tilde{u}_2 & \bar{\rho}\tilde{u}_1\tilde{u}_3 \\ \bar{\rho}\tilde{u}_1\tilde{u}_2 & \bar{\rho}\tilde{u}_2\tilde{u}_2 + \bar{p} & \bar{\rho}\tilde{u}_2\tilde{u}_3 \\ \bar{\rho}\tilde{u}_1\tilde{u}_3 & \bar{\rho}\tilde{u}_2\tilde{u}_3 & \bar{\rho}\tilde{u}_3\tilde{u}_3 + \bar{p} \\ \tilde{u}_1(\bar{\rho}\tilde{E} + \bar{p}) & \tilde{u}_2(\bar{\rho}\tilde{E} + \bar{p}) & \tilde{u}_3(\bar{\rho}\tilde{E} + \bar{p}) \end{bmatrix} \tag{12}$$

is the tensor of convective terms and

$$\mathbf{G}_v^k \equiv \begin{bmatrix} \mathbf{G}_v^1 & \mathbf{G}_v^2 & \mathbf{G}_v^3 \end{bmatrix} = \begin{bmatrix} 0 & 0 & 0 \\ \bar{\sigma}_{11} + \tau_{11} & \bar{\sigma}_{12} + \tau_{12} & \bar{\sigma}_{13} + \tau_{13} \\ \bar{\sigma}_{21} + \tau_{21} & \bar{\sigma}_{22} + \tau_{22} & \bar{\sigma}_{23} + \tau_{23} \\ \bar{\sigma}_{31} + \tau_{31} & \bar{\sigma}_{32} + \tau_{32} & \bar{\sigma}_{33} + \tau_{33} \\ G_{v5,1} & G_{v5,2} & G_{v5,3} \end{bmatrix} \tag{13}$$

is the tensor of diffusive terms, with

$$G_{v5,1} = u_1\bar{\sigma}_{11} + u_2\bar{\sigma}_{12} + u_3\bar{\sigma}_{13} - \bar{q}_1 - \overline{p''u_1''} + \overline{u_1''\sigma_{11}''} + \overline{u_2''\sigma_{12}''} + \overline{u_3''\sigma_{13}''} - \bar{\rho}\widetilde{E'u_1'},$$

$$G_{v5,2} = u_1\bar{\sigma}_{21} + u_2\bar{\sigma}_{22} + u_3\bar{\sigma}_{23} - \bar{q}_2 - \overline{p''u_2''} + \overline{u_1''\sigma_{21}''} + \overline{u_2''\sigma_{22}''} + \overline{u_3''\sigma_{23}''} - \bar{\rho}\widetilde{E'u_2'},$$

$$G_{v5,3} = u_1\bar{\sigma}_{31} + u_2\bar{\sigma}_{32} + u_3\bar{\sigma}_{33} - \bar{q}_3 - \overline{p''u_3''} + \overline{u_1''\sigma_{31}''} + \overline{u_2''\sigma_{32}''} + \overline{u_3''\sigma_{33}''} - \bar{\rho}\widetilde{E'u_3'}.$$

3. TURBULENCE MODELS

The terms $-\bar{\rho}\widetilde{u_i'u_j'}$, $\overline{\sigma_{jk}''u_j''}$, $\overline{p''u_k''}$, $\widetilde{T'u_k'}$ and $\widetilde{u_j'u_j'u_k'}/2$ in the mean equations are not known or expressible in terms of the solution variables. Thus models have to be given to assign values to them or to express them in terms of the solution variables. The Reynolds/Favre-averaged transport equations are solved for the Reynolds stress tensor, for which the equations are given by

$$\frac{\partial}{\partial t}(\bar{\rho}\widetilde{u_i'u_j'}) + \frac{\partial}{\partial x_k}(\bar{\rho}\tilde{u}_k\widetilde{u_i'u_j'}) = P_{ij} + \Pi_{ij} - \frac{\partial T_{ijk}}{\partial x_k} - \bar{\rho}\varepsilon_{ij} + \frac{2}{3}\overline{p''\frac{\partial u_k''}{\partial x_k}}\delta_{ij} - \overline{u_i'}\frac{\partial \bar{p}}{\partial x_j} - \overline{u_j'}\frac{\partial \bar{p}}{\partial x_i} + \overline{u_i'}\frac{\partial \bar{\sigma}_{jk}}{\partial x_k} + \overline{u_j'}\frac{\partial \bar{\sigma}_{ik}}{\partial x_k}, \tag{14}$$

where

$$P_{ij} = -\bar{\rho}\left(\widetilde{u_i'u_k'}\frac{\partial u_j}{\partial x_k} + \widetilde{u_j'u_k'}\frac{\partial \bar{u}_i}{\partial x_k}\right), \qquad \Pi_{ij} = \overline{p''\frac{\partial u_i''}{\partial x_j}} + \overline{p''\frac{\partial u_j''}{\partial x_i}} - \frac{2}{3}\overline{p''\frac{\partial u_k''}{\partial x_k}}\delta_{ij},$$

$$T_{ijk} = \bar{\rho}\widetilde{u_i'u_j'u_k'} + (\overline{p''u_i''}\,\delta_{jk} + \overline{p''u_j''}\,\delta_{ik}) - (\overline{\sigma_{ik}''u_j''} + \overline{\sigma_{ik}''u_j''}),$$

$$\varepsilon_{ij} = \overline{\sigma_{ik}''\frac{\partial u_j''}{\partial x_k}} + \overline{\sigma_{jk}''\frac{\partial u_i''}{\partial x_k}}.$$

In equation (14), from left to right, we have the time rate of change of the Reynolds stress at a fixed point, the net convection of Reynolds stress by the mean flow to the fixed point, the local production (P_{ij}) of Reynolds stress, the local pressure–strain (Π_{ij}), the net diffusive transport ($T_{ijk,k}$) of Reynolds stress to the fixed point, the local dissipation tensor (ε_{ij}, solenoidal plus compressible) and the local pressure–dilatation. The last four terms represent the 'production' of Reynolds stress at the fixed point by the Favre (mass)-averaged velocity. In these equations the time rate of change of the Reynolds stress, the convective terms and the production terms are closed, whereas $\Pi_{ij}, T_{ijk,k}, \varepsilon_{ij}$, the pressure–dilatation and the mass-averaged velocity terms are unclosed.

Some of the unclosed terms in these equations are modelled using the variable density extension of the incompressible models. Such is the case for all terms that do not contain the divergence $u_{j,j}$, with the exception of the Favre velocity terms which have no analogy in incompressible flows. Terms with divergence and the Favre-velocity terms are modelled from compressible turbulence considerations.

The model we have used for the dissipation rate tensor is[29]

$$\varepsilon_{ij} = \bar{\rho}\frac{\varepsilon}{k}[\widetilde{u_i'u_j'}f_s + \tfrac{2}{3}(1 - f_s)k\delta_{ij}], \tag{15}$$

where f_s is a function of the turbulent Reynolds number $R_t = k^2/\nu\varepsilon$ and is given by $f_s = 10/(10 + R_t)$. This model contracts to 2ε at the wall, meaning that it has the correct asymptotic behaviour at the wall.[30]

The transport equation we have used for the solenoidal dissipation is based on a variable density extension of the incompressible model of Hanjalic and Launder:[31]

$$\frac{\partial(\bar{\rho}\varepsilon_s)}{\partial t}+\frac{\partial(\bar{\rho}\tilde{u}_k\varepsilon_s)}{\partial x_k}=-C_{\varepsilon_1}\frac{\varepsilon_s}{k}\bar{\rho}\widetilde{u_i'u_j'}\frac{\partial\tilde{u}_i}{\partial x_j}-C_{\varepsilon_2}\bar{\rho}\frac{\varepsilon_s^2}{k}+\frac{\partial}{\partial x_k}\left(C_\varepsilon\frac{\bar{\rho}k}{\varepsilon_s}\widetilde{u_k'u_l'}\frac{\partial\varepsilon_s}{\partial x_l}\right), \tag{16}$$

where the constants are $C_\varepsilon = 0{\cdot}18$, $C_{\varepsilon_1} = 1{\cdot}44$, $C_{\varepsilon_2} = 1{\cdot}9$. The wall value for ε_s is $(\varepsilon_s)_w = 2\nu(\partial k^{1/2}/\mathrm{d}y)^2$.

The model for the pressure–strain correlation Π_{ij} is[32]

$$\Pi_{ij}=\underbrace{-C_1\bar{\rho}\varepsilon b_{ij}}_{\text{slow term}}-\underbrace{C_2\left(P_{ij}-\frac{P_{kk}}{3}\delta_{ij}\right)}_{\text{fast term}}\equiv\Pi_{ij}^1+\Pi_{ij}^2, \tag{17}$$

where

$$b_{ij}=\frac{\widetilde{u_i'u_j'}}{q^2}-\frac{\delta_{ij}}{3} \tag{18}$$

is the anisotropy tensor and $q^2=\widetilde{u_k'u_k'}=2k$ denotes the trace of the Reynolds stress tensor; k is the kinetic energy of turbulence. A new model that incorporates the effect of Mach number has been proposed for the fast term[33] but has not been thoroughly tested. We include wall effects in the pressure–strain by assuming the model of Launder and Shima:[34]

$$\Pi_{ij}^{\mathrm{w}}=\left(\Pi_{ij}^{\mathrm{w},1}+\Pi_{ij}^{\mathrm{w},2}\right)f\left(\frac{l}{y_in_i}\right), \tag{19}$$

where the slow wall correction term is given by

$$\Pi_{ij}^{\mathrm{w},1}=C_1'\frac{\varepsilon\bar{\rho}}{k}\left[\widetilde{u_k'u_m'}n_kn_m\delta_{ij}-\tfrac{3}{2}(\widetilde{u_k'u_i'}n_kn_j+\widetilde{u_k'u_j'}n_kn_i)\right] \tag{20}$$

and the fast wall correction term is given by

$$\Pi_{ij}^{\mathrm{w},2}=C_2'\left[\Pi_{km}^2n_kn_m\delta_{ij}-\tfrac{3}{2}(\Pi_{ik}^2n_kn_j+\Pi_{jk}^2n_kn_i)\right]. \tag{21}$$

The near-wall damping function f is normalized to unity in the fully turbulent region of a turbulent boundary layer. The quantity y_in_i is the normal distance to the wall, with y_i representing the Cartesian wall position vector having a unit normal vector n_i. The quantity l represents the turbulent length scale of the flow, which is estimated to be

$$l=k^{3/2}/\varepsilon.$$

Launder and Shima[34] have shown the near-wall damping function f to be

$$f\left(\frac{l}{y_in_i}\right)=0.41\frac{k^{3/2}}{\varepsilon y_in_i}. \tag{22}$$

The constants C_1' and C_2', taken from Reference 35, are $C_1' = 0{\cdot}5$ and $C_2' = 0{\cdot}3$.

The transport term $T_{ijk,k}$ consists of three parts, i.e.

$$T_{ijk,k}=\underbrace{C_{ijk,k}}_{\text{turbulent diffusion}}+\underbrace{E_{ijk,k}}_{\text{pressure diffusion}}-\underbrace{D_{ijk,k}}_{\text{viscous diffusion}}.$$

The model for the triple correlation $C_{ijk,k} \equiv \widetilde{\rho u_i'' u_j'' u_k''}$, is[31]

$$C_{ijk,k} = \frac{\partial}{\partial x_k}\left[-C_s\bar{\rho}\,\frac{(q^2)^2}{\varepsilon}\left(\frac{\partial(\widetilde{u_i'' u_j''})}{\partial x_k} + \frac{\partial(\widetilde{u_j'' u_k''})}{\partial x_i} + \frac{\partial(\widetilde{u_i'' u_k''})}{\partial x_j}\right)\right] \tag{23}$$

The model coefficient $C_s = 0{\cdot}018$. We will assume that pressure diffusion effects are included in the model for the triple correlation, as did Hanjalic and Launder.[31] The various other models proposed for pressure diffusion have not performed significantly better than the one used here.[36]

The viscous diffusion term is modelled according to Launder and Shima[34] and is given by

$$D_{ijk,k} = \frac{\partial}{\partial x_k}\left(\bar{\mu}\,\frac{\partial \widetilde{u_i'' u_j''}}{\partial x_k}\right). \tag{24}$$

The Favre-averaging procedure introduces the quantity $\overline{u_i''}$ which does not appear in the incompressible form of the Reynolds transport equation. Gradient transport is assumed:

$$\overline{u_i''} = -\frac{\overline{\rho'' u_i''}}{\bar{\rho}} = \frac{C_\mu k^2}{\bar{\rho}\varepsilon\sigma_p}\,\frac{\partial \bar{\rho}}{\partial x_i}. \tag{25}$$

The model constant $C_\mu = 0{\cdot}09$ is taken from Reference 37, while the turbulent Schmidt number $\sigma_p = 0{\cdot}7$.

The turbulent quantities that need to be closed in the mean energy equation are

$$\overline{\sigma_{jk}'' u_j''}, \quad \overline{p'' u_k''}, \quad \frac{\widetilde{u_j'' u_j'' u_k''}}{2}, \quad \widetilde{T'' u_k''}.$$

From the definition of the transport term in the Reynolds stress transport equation the quantities $\overline{\sigma_{jk}'' u_j''}$, $\overline{p'' u_k''}$ and $\widetilde{u_j'' u_j'' u_k''}/2$ can be combined to yield

$$\overline{\sigma_{jk}'' u_j''} - \overline{p'' u_k''} - \frac{\widetilde{u_j'' u_j'' u_k''}}{2} = -\frac{T_{ijk}}{2}.$$

Thus the same models in the Reynolds stress transport equation can be employed for the corresponding terms in the mean energy equation.

Concerning $\widetilde{T'' u_k''}$, evolution equations can be written[38] which introduce three additional transport equations. For simplicity we use gradient transport as in Reference 37:

$$\widetilde{T'' u_k''} = -\frac{C_\mu k^2}{\varepsilon\sigma_T}\,\frac{\partial \tilde{T}}{\partial x_k}, \tag{26}$$

where $\sigma_T = 0{\cdot}7$ is the turbulent Prandtl number.

Sarkar *et al.*[39] and Zeman[40] have suggested that for large Reynolds numbers, ε in equation (15) consists of two parts, i.e.

$$\varepsilon = \varepsilon_s + \varepsilon_d, \tag{27}$$

where ε_s represents the solenoidal dissipation and ε_d represents the compressible dissipation:

$$\varepsilon_s = \bar{\nu}\overline{\omega_i'' \omega_i''}, \qquad \varepsilon_d = \tfrac{4}{3}\bar{\nu}\overline{d''^2}. \tag{28}$$

Here $d'' \equiv u_{k,k}''$ denotes the fluctuating dilatation and $\omega_i'' = \varepsilon_{ijk} u_{k,j}''$ represents the fluctuating vorticity, where ε_{ijk} is the permutation tensor. Models for ε_d are based on the assumption that the compressible dissipation is a function of the turbulent Mach number. Zeman's approach[40] assumes the existence of shock-like structures embedded within the energetic turbulent eddies, while Sarkar *et al.*[39] use low-

Mach-number asymptotics to obtain a scaling relation. With Sarkar *et al.*'s model, $\varepsilon_d = M_t^2$, where $M_t = q^2/c^2$ is the turbulent Mach number, $c = \sqrt{(\gamma \bar{p}/\bar{\rho})}$ is the speed of sound and q^2 is twice the turbulent kinetic energy $\widetilde{u_i' u_i'}$. Zeman's model is more general, as it incorporates intermittency and dependence on γ, the ratio of specific heats. One form of Zeman's model is

$$\varepsilon_d = \varepsilon_s c_d \left\{ 1 - \exp\left[-\left(\frac{M_{t^*} - M_{t_0}}{\sigma_M} \right)^2 \right] \right\},$$

where $\varepsilon_d = 0$ if $M_t * \leq M_{t_0}$, with $M_{t_0} = 0{\cdot}2$, $\sigma_M = 0{\cdot}66$, $c_d = 0{\cdot}75$ and

$$M_{t^*} = \sqrt{\left(\frac{2}{\gamma + 1} \right)} M_t.$$

We are experimenting with these two models for ε_d, although the results presented here were obtained using that of Sarkar *et al.*

With the foregoing, the final form of the turbulence equations can be written as

$$\frac{\partial \mathbf{q}_{rs}}{\partial t} + \frac{\partial \mathbf{G}_{rs}^k}{\partial x_k} = \mathbf{S}_{rs1} + \mathbf{S}_{rs2} + \frac{\partial \mathbf{D}_{rs}^k}{\partial x_k}, \tag{29}$$

where

$$\mathbf{q}_{rs} = \begin{bmatrix} \bar{\rho}\widetilde{u_1' u_1'} \\ \bar{\rho}\widetilde{u_1' u_2'} \\ \bar{\rho}\widetilde{u_1' u_3'} \\ \bar{\rho}\widetilde{u_2' u_2'} \\ \bar{\rho}\widetilde{u_2' u_3'} \\ \bar{\rho}\widetilde{u_3' u_3'} \\ \bar{\rho}\varepsilon_s \end{bmatrix}$$

is the vector of unknown stresses,

$$\mathbf{G}_{rs}^k \equiv \begin{bmatrix} \mathbf{G}_{rs}^1 & \mathbf{G}_{rs}^2 & \mathbf{G}_{rs}^3 \end{bmatrix} = \begin{bmatrix} \bar{\rho}\widetilde{u_1' u_1'}\tilde{u}_1 & \bar{\rho}\widetilde{u_1' u_1'}\tilde{u}_2 & \bar{\rho}\widetilde{u_1' u_1'}\tilde{u}_3 \\ \bar{\rho}\widetilde{u_1' u_2'}\tilde{u}_1 & \bar{\rho}\widetilde{u_1' u_2'}\tilde{u}_2 & \bar{\rho}\widetilde{u_1' u_2'}\tilde{u}_3 \\ \bar{\rho}\widetilde{u_1' u_3'}\tilde{u}_1 & \bar{\rho}\widetilde{u_1' u_3'}\tilde{u}_2 & \bar{\rho}\widetilde{u_1' u_3'}\tilde{u}_3 \\ \bar{\rho}\widetilde{u_2' u_2'}\tilde{u}_1 & \bar{\rho}\widetilde{u_2' u_2'}\tilde{u}_2 & \bar{\rho}\widetilde{u_2' u_2'}\tilde{u}_3 \\ \bar{\rho}\widetilde{u_2' u_3'}\tilde{u}_1 & \bar{\rho}\widetilde{u_2' u_3'}\tilde{u}_2 & \bar{\rho}\widetilde{u_2' u_3'}\tilde{u}_3 \\ \bar{\rho}\widetilde{u_3' u_3'}\tilde{u}_1 & \bar{\rho}\widetilde{u_3' u_3'}\tilde{u}_2 & \bar{\rho}\widetilde{u_3' u_3'}\tilde{u}_3 \\ \bar{\rho}\varepsilon_s\tilde{u}_1 & \bar{\rho}\varepsilon_s\tilde{u}_2 & \bar{\rho}\varepsilon_s\tilde{u}_3 \end{bmatrix}$$

is the tensor of convective terms,

$$\mathbf{S}_{rs1} = \begin{bmatrix} P_{11} + \Pi_{11} - \varepsilon_{11} + \Pi_{11}^w \\ P_{12} + \Pi_{12} - \varepsilon_{12} + \Pi_{12}^w \\ P_{13} + \Pi_{13} - \varepsilon_{13} + \Pi_{13}^w \\ P_{22} + \Pi_{22} - \varepsilon_{22} + \Pi_{22}^w \\ P_{23} + \Pi_{23} - \varepsilon_{23} + \Pi_{23}^w \\ P_{33} + \Pi_{33} - \varepsilon_{33} + \Pi_{33}^w \\ -C_{\varepsilon_1} \dfrac{\varepsilon_s}{k} \left(\dfrac{P_{11} + P_{22} + P_{33}}{2} \right) - C_{\varepsilon_2} \bar{\rho} \dfrac{\varepsilon_s}{k} \end{bmatrix}$$

and

$$\mathbf{S}_{rs2} = \begin{bmatrix} \overline{u_1'}(\bar{\sigma}_{11,1} + \bar{\sigma}_{12,2} + \sigma_{13,3}) - \overline{u_1'}\dfrac{\partial \bar{p}}{\partial x} + \overline{u_1'}(\bar{\sigma}_{11,1} + \bar{\sigma}_{12,2} + \bar{\sigma}_{13,3}) - \overline{u_1'}\dfrac{\partial \bar{p}}{\partial x} \\ \overline{u_1'}(\bar{\sigma}_{21,1} + \bar{\sigma}_{22,2} + \sigma_{23,3}) - \overline{u_1'}\dfrac{\partial \bar{p}}{\partial y} + \overline{u_2'}(\bar{\sigma}_{11,1} + \bar{\sigma}_{12,2} + \bar{\sigma}_{13,3}) - \overline{u_2'}\dfrac{\partial \bar{p}}{\partial x} \\ \overline{u_1'}(\bar{\sigma}_{31,1} + \bar{\sigma}_{32,2} + \sigma_{33,3}) - \overline{u_1'}\dfrac{\partial \bar{p}}{\partial z} + \overline{u_3'}(\bar{\sigma}_{11,1} + \bar{\sigma}_{12,2} + \bar{\sigma}_{13,3}) - \overline{u_3'}\dfrac{\partial \bar{p}}{\partial x} \\ \overline{u_2'}(\bar{\sigma}_{21,1} + \bar{\sigma}_{22,2} + \sigma_{23,3}) - \overline{u_2'}\dfrac{\partial \bar{p}}{\partial y} + u_2'(\bar{\sigma}_{21,1} + \bar{\sigma}_{22,2} + \bar{\sigma}_{23,3}) - \overline{u_2'}\dfrac{\partial \bar{p}}{\partial y} \\ \overline{u_2'}(\bar{\sigma}_{31,1} + \bar{\sigma}_{32,2} + \sigma_{33,3}) - \overline{u_2'}\dfrac{\partial \bar{p}}{\partial z} + \overline{u_3'}(\bar{\sigma}_{21,1} + \bar{\sigma}_{22,2} + \bar{\sigma}_{23,3}) - \overline{u_3'}\dfrac{\partial \bar{p}}{\partial y} \\ \overline{u_3'}(\bar{\sigma}_{11,1} + \bar{\sigma}_{12,2} + \sigma_{13,3}) - \overline{u_3'}\dfrac{\partial \bar{p}}{\partial z} + \overline{u_3'}(\bar{\sigma}3_{11,1} + \bar{\sigma}_{32,2} + \bar{\sigma}_{33,3}) - \overline{u_3'}\dfrac{\partial \bar{p}}{\partial z} \\ 0 \end{bmatrix}$$

are source vectors and

$$\mathbf{D}_{rs}^{k} = \begin{bmatrix} \mathbf{D}_{rs}^{1} & \mathbf{D}_{rs}^{2} & \mathbf{D}_{rs}^{3} \end{bmatrix} = \begin{bmatrix} -T_{111} & -T_{112} & -T_{113} \\ -T_{121} & -T_{122} & -T_{123} \\ -T_{131} & -T_{132} & -T_{133} \\ -T_{221} & -T_{222} & -T_{223} \\ -T_{231} & -T_{232} & -T_{233} \\ -T_{331} & -T_{332} & -T_{333} \\ D_{rs7,1} & D_{rs7,2} & D_{rs7,3} \end{bmatrix}$$

is the tensor of diffusive terms, with

$$D_{rs7,1} = C_\varepsilon \frac{\bar{\rho} k}{\varepsilon_s}\left(\widetilde{u_1'u_1'}\frac{\partial \varepsilon_s}{\partial x} + \widetilde{u_1'u_2'}\frac{\partial \varepsilon_s}{\partial y} + \widetilde{u_1'u_3'}\frac{\partial \varepsilon_s}{\partial z}\right),$$

$$D_{rs7,2} = C_\varepsilon \frac{\bar{\rho} k}{\varepsilon_s}\left(\widetilde{u_1'u_2'}\frac{\partial \varepsilon_s}{\partial x} + \widetilde{u_2'u_2'}\frac{\partial \varepsilon_s}{\partial y} + \widetilde{u_2'u_3'}\frac{\partial \varepsilon_s}{\partial z}\right),$$

$$D_{rs7,3} = C_\varepsilon \frac{\bar{\rho} k}{\varepsilon_s}\left(\widetilde{u_1'u_3'}\frac{\partial \varepsilon_s}{\partial x} + \widetilde{u_2'u_3'}\frac{\partial \varepsilon_s}{\partial y} + \widetilde{u_3'u_3'}\frac{\partial \varepsilon_s}{\partial z}\right),$$

Initial conditions and boundary conditions will be discussed under specific sample calculations.

4. NUMERICAL PROCEDURE

Our procedure is a finite volume one in which FVS and FDS are combined, as discussed earlier in this paper. We start by applying the divergence theorem to equation (10) to obtain

$$\int_V \frac{\partial \mathbf{q}}{\partial t}\,dV + \int_S \mathbf{F}\,dS = \int_S \mathbf{F}_v\,dS, \tag{30}$$

where $\mathbf{F} \equiv \mathbf{G}^k n^k$, $\mathbf{F}_v \equiv \mathbf{G}\mathbf{v}^k n^k$ and dS is an element of a surface having an outward normal n^k.

A cell-centered finite volume is used, where the vector of dependent variables, $\mathbf{q}$ or $\mathbf{q}_{rs}$, is assumed

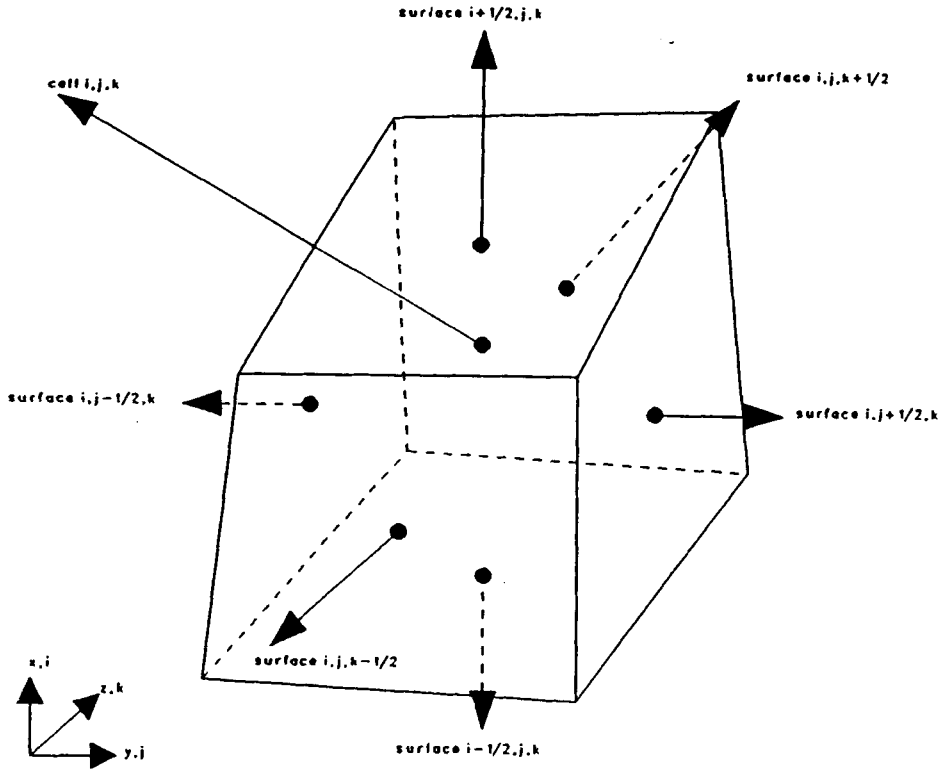

Figure 1. A typical finite volume cell showing the index notation. The notation (i,j,k) refers to the cell centroid where the primary variables are solved, while fractional indices such as $(i+\frac{1}{2},j,k)$ refer to control volume surfaces

to 'reside' at the centroid of the cell. The index convention is shown in Figure 1. If the fluxes $\mathbf{F}$ and $\mathbf{F}_v$ are assumed constant over each cell surface, the integrals above can be approximated by the implicit equation

$$V\frac{\partial \mathbf{q}}{\partial t}+\sum_{l=1}^{6}(\mathbf{F}^{n+1}S)_l=\sum_{l=1}^{6}(\mathbf{F}_v^{n+1}S)_l. \tag{31}$$

The procedure for calculating surface areas and cell volumes is discussed later in the paper. Euler time integration of equation (31) gives

$$\Delta\mathbf{q}^n+\frac{\Delta t}{V}\sum_{l=1}^{6}(\mathbf{F}^{n+1}S)_l=\frac{\Delta t}{V}\sum_{l=1}^{6}(\mathbf{F}_v^{n+1}S)_l, \tag{32}$$

where $\Delta\mathbf{q}^n=\mathbf{q}^{n+1}-\mathbf{q}^n$.

Beam–Warming[41] linearization gives

$$\mathbf{F}^{n+1}=\mathbf{F}^n+(\mathbf{A}\Delta\mathbf{q})^n+O(\Delta t^2). \tag{32}$$

In the FDS scheme the exact Jacobian of the Roe matrix is too expensive to compute and approximated Jacobians have been observed to give poor convergence compared with FVS.[13] In the present work the FVS scheme is used to evaluate the Jacobians in the implicit part (left-hand side) of the matrix equation (38) (below) for $\Delta\mathbf{q}$. The Euler flux $\mathbf{F}^n$ in the residual part (right-hand side) is computed using the FDS scheme. With FDS via Roe splitting,[42] the flux at the surface is evaluated as

$$\mathbf{F}^n \equiv \mathbf{F} = \frac{\mathbf{F}_{i,j,k} + \mathbf{F}_{i+1,j,k}}{2} - \tfrac{1}{2} \sum_1^5 \alpha_k |\lambda_k| \mathbf{R}_k. \tag{34}$$

Here λ_k are the characteristic wave speeds of the Riemann problem and α_k represents the projection of $\Delta\mathbf{q}$ onto the eigenvectors of Roe's approximate Jacobian, obtainable from $\Delta\mathbf{q} = \sum_1^5 \alpha_k \mathbf{R}_k$. $\mathbf{R}_k$ are the right eigenvectors of Roe's matrix. The fluxes $\mathbf{F}_{i+1,j,k}$ and $\mathbf{F}_{i,j,k}$ in equation (34) are evaluated using the conserved variables $\mathbf{q}_{i+1,j,k}$ and $\mathbf{q}_{i,j,k}$ respectively. Following Frink,[43] the sum $\sum_1^5 \alpha_k |\lambda_k| \mathbf{R}_k$ is written in terms of five flux jumps $\Delta\mathbf{F}_k$, each associated with a distinct eigenvalue $\tilde{\lambda}_k$, of Roe's matrix.

For the FVS technique

$$(\mathbf{F}^{\pm})^{n+1} = (\mathbf{F}^{\pm})^n + (\mathbf{A}^{\pm}\Delta\mathbf{q})^n, \tag{35}$$

where the plus and minus signs indicate evaluation based on the negative and positive eigenvalues of matrix $\mathbf{A}$ respectively. In terms of the centroid values, surface quantities are approximated e.g. by

$$(\mathbf{A}\Delta\mathbf{q})^n_{i+1/2,j,k} = (\mathbf{A}^+\Delta\mathbf{q})^n_{i,j,k} + (\mathbf{A}^-\Delta\mathbf{q})^n_{i+1,j,k}. \tag{36}$$

The diffusive flux is linearized as

$$\mathbf{F}_{\mathrm{v}}^{n+1} = \mathbf{F}_{\mathrm{v}}^n + O(\Delta t) \tag{37}$$

and treated explicitly to preserve the upwinding scheme.

Substitution of equations (35)–(37) into equation (32) yields the matrix system

$$\begin{aligned}
&\Bigg(\mathbf{I} + \frac{\Delta t}{V}\big[(\mathbf{A}^+)^n_{i,j,k} S_{i+1/2,j,k} \bullet + (\mathbf{A}^+)^n_{i,j,k} S_{i,j+1/2,k} \bullet + (\mathbf{A}^+)^n_{i,j,k} S_{i,j,k+1/2} \bullet \\
&\quad + (\mathbf{A}^+)^n_{i-1,j,k} S_{i-1/2,j,k} \bullet + (\mathbf{A}^+)^n_{i,j-1,k} S_{i,j-1/2,k} \bullet + (\mathbf{A}^+)^n_{i,j,k-1} S_{i,j,k-1/2} \bullet \\
&\quad + (\mathbf{A}^-)^n_{i,j,k} S_{i-1/2,j,k} \bullet + (\mathbf{A}^-)^n_{i,j,k} S_{i,j-1/2,k} \bullet + (\mathbf{A}^-)^n_{i,j,k} S_{i,j,k-1/2} \bullet \\
&\quad + (\mathbf{A}^-)^n_{i+1,j,k} S_{i+1/2,j,k} \bullet + (\mathbf{A}^-)^n_{i,j+1,k} S_{i,j+1/2,k} \bullet + (\mathbf{A}^-)^n_{i,j,k+1} S_{i,j,k+1/2} \bullet\big]\Bigg) \Delta\mathbf{q}^n \\
&\qquad = -\frac{\Delta t}{V}\left(\sum_{l=1}^{6} (\mathbf{F}^n S)_l - \sum_{l=1}^{6} (\mathbf{F}_{\mathrm{v}}^n S)_l\right) \equiv -\frac{\Delta t}{V}\mathbf{R}^n,
\end{aligned} \tag{38}$$

where '$\bullet$' indicates that e.g. the term $(\mathbf{A}^-)^n_{i+1,j,k} S_{i+1/2,j,k}$ acts on $(\Delta\mathbf{q}^n)_{i+1,j,k}$. Furthermore, equation (38) is a matrix–vector equation, so that each term is a vector after carrying out the multiplications. The indices i,j,k are used to denote grid points in the local directions i,j,k, in which (i,j,k) is the centroid of a cell and half-indices such as $i+1/2$ denote the surface of the cell (see Figure 1). When a scalar, vector or matrix is subscripted with these indices, we imply that the scalar or each element of the vector or matrix is to be evaluated at the point or surface indicated by the indices. Note that the symbol S in equation (38) is a scalar which denotes the area of the surface indicated by the subscripts.

It is impractical to solve equation (38) because the bandwidth of the resulting matrix system is too large. Many different techniques are used to simplify the task. The most common of these are the alternating direction implicit (ADI)[44] method and the lower–upper (LU) decomposition method (to be discussed later). Jameson *et al.* have compared these two methods and observed that (i) LU decomposition is more advantageous for three-dimensional calculations because only two passes through the domain are used while the ADI method requires three, (ii) the LU method is unconditionally stable while the ADI method is unconditionally unstable and (iii) the LU method converges faster than the ADI method for the same time step. LU decomposition is used in this paper.

In the LU method employed in the present work the coefficient matrix in equation (38) is split into two factors, one corresponding to all positive eigenvalues (lower block) and the other corresponding to all negative eigenvalues (upper block). The resulting factored equation is

$$\left(\mathbf{I}+\frac{\Delta t}{V}[(\mathbf{A}^{+})^{n}_{i,j,k}S_{i+1/2,j,k}\bullet+(\mathbf{A}^{+})^{n}_{i,j,k}S_{i,j+1/2,k}\bullet+(\mathbf{A}^{+})^{n}_{i,j,k}S_{i,j,k+1/2}\bullet\right.$$
$$+(\mathbf{A}^{+})^{n}_{i-1,j,k}S_{i-1/2,j,k}\bullet+(\mathbf{A}^{+})^{n}_{i,j-1,k}S_{i,j-1/2,k}\bullet+(\mathbf{A}^{+})^{n}_{i,j,k-1}S_{i,j,k-1/2}\bullet]\Big)$$
$$\times\left(\mathbf{I}+\frac{\Delta t}{V}[(\mathbf{A}^{-})^{n}_{i,j,k}S_{i-1/2,j,k}\bullet+(\mathbf{A}^{-})^{n}_{i,j,k}S_{i,j-1/2,k}\bullet+(\mathbf{A}^{-})^{n}_{i,j,k}S_{i,j,k-1/2}\bullet\right.$$
$$+(\mathbf{A}^{-})^{n}_{i+1,j,k}S_{i+1/2,j,k}\bullet+(\mathbf{A}^{-})^{n}_{i,j+1,k}S_{i,j+1/2,k}\bullet+(\mathbf{A}^{-})^{n}_{i,j,k+1}S_{i,j,k+1/2}\bullet]\Big)\Delta\mathbf{q}^{n}$$
$$=-\frac{\Delta t}{V}\mathbf{R}^{n}. \tag{39}$$

The factorization error is of $O(\Delta t^2)$.

The solution to equation (39) is carried out as follows.

Forward sweep

$$\left(\mathbf{I}+\frac{\Delta t}{V}[(\mathbf{A}^{+})^{n}_{i,j,k}S_{i+1/2,j,k}\bullet+(\mathbf{A}^{+})^{n}_{i,j,k}S_{i,j+1/2,k}\bullet+(\mathbf{A}^{+})^{n}_{i,j,k}S_{i,j,k+1/2}\bullet\right.$$
$$+(\mathbf{A}^{+})^{n}_{i-1,j,k}S_{i-1/2,j,k}\bullet+(\mathbf{A}^{+})^{n}_{i,j-1,k}S_{i,j-1/2,k}\bullet+(\mathbf{A}^{+})^{n}_{i,j,k-1}S_{i,j,k-1/2}\bullet]\Big)\Delta\mathbf{w}^{n}$$
$$=-\frac{\Delta t}{V}\mathbf{R}^{n}. \tag{40}$$

A sparse block lower tridiagonal matrix is solved using forward substitution. Because boundary conditions are treated explicitly, $\Delta\mathbf{w}^n$ is set to zero at the 'left' and 'bottom' boundaries of the domain.

Backward sweep

$$\left(\mathbf{I}+\frac{\Delta t}{V}[(\mathbf{A}^{-})^{n}_{i,j,k}S_{i-1/2,j,k}\bullet+(\mathbf{A}^{-})^{n}_{i,j,k}S_{i,j-1/2,k}\bullet+(\mathbf{A}^{-})^{n}_{i,j,k}S_{i,j,k-1/2}\bullet\right.$$
$$+(\mathbf{A}^{-})^{n}_{i+1,j,k}S_{i+1/2,j,k}\bullet+(\mathbf{A}^{-})^{n}_{i,j+1,k}S_{i,j+1/2,k}\bullet+(\mathbf{A}^{-})^{n}_{i,j,k+1}S_{i,j,k+1/2}\bullet]\Big)\Delta\mathbf{q}^{n}$$
$$=\Delta\mathbf{w}^{n}. \tag{41}$$

A sparse upper tridiagonal matrix is solved using backward substitution. At the 'right' and 'top' boundaries of the domain, $\Delta\mathbf{q}^n$ is set to zero for the same reason given above.

Update solution

$$\mathbf{q}^{n+1}=\mathbf{q}^{n}+\Delta\mathbf{q}^{n}. \tag{42}$$

For the turbulence the analogous equations to (38) and (40)–(42) are

$$\left(\mathbf{I}+\frac{\Delta t}{V}[(\mathbf{A}^{+}_{\mathrm{rs}})^{n}_{i,j,k}S_{i+1/2,j,k}\bullet+(\mathbf{A}^{+}_{\mathrm{rs}})^{n}_{i,j,k}S_{i,j+1/2,k}\bullet+(\mathbf{A}^{+}_{\mathrm{rs}})^{n}_{i,j,k}S_{i,j,k+1/2}\bullet\right.$$
$$+(\mathbf{A}^{+}_{\mathrm{rs}})^{n}_{i-1,j,k}S_{i-1/2,j,k}\bullet+(\mathbf{A}^{+}_{\mathrm{rs}})^{n}_{i,j-1,k}S_{i,j-1/2,k}\bullet+(\mathbf{A}^{+}_{\mathrm{rs}})^{n}_{i,j,k-1}S_{i,j,k-1/2}\bullet$$
$$+(\mathbf{A}^{-}_{\mathrm{rs}})^{n}_{i,j,k}S_{i-1/2,j,k}\bullet+(\mathbf{A}^{-}_{\mathrm{rs}})^{n}_{i,j,k}S_{i,j-1/2,k}\bullet+(\mathbf{A}^{-}_{\mathrm{rs}})^{n}_{i,j,k}S_{i,j,k-1/2}\bullet$$
$$+(\mathbf{A}^{-}_{\mathrm{rs}})^{n}_{i+1,j,k}S_{i+1/2,j,k}\bullet+(\mathbf{A}^{-}_{\mathrm{rs}})^{n}_{i,j+1,k}S_{i,j+1/2,k}\bullet+(\mathbf{A}^{-}_{\mathrm{rs}})^{n}_{i,j,k+1}S_{i,j,k+1/2}\bullet]\Big)\Delta\mathbf{q}^{n}_{\mathrm{rs}}$$
$$=\frac{\Delta t}{V}\left(\sum_{l=1}^{6}(\mathbf{E}^{n}_{\mathrm{rs}}S)_{l}-\sum_{l=1}^{6}[(\mathbf{F}^{+}_{\mathrm{rs}})^{n}S]_{l}-\sum_{l=1}^{6}[(\mathbf{F}^{-}_{\mathrm{rs}})^{n}S]_{l}+\mathbf{S}^{n}_{\mathrm{rs1}}V+\mathbf{S}^{n}_{\mathrm{rs2}}V\right)\equiv\frac{\Delta t}{V}\mathbf{R}^{n}_{\mathrm{rs}}; \tag{43}$$

forward sweep,

$$\left(\mathbf{I}+\frac{\Delta t}{V}[(\mathbf{A}_{\mathrm{rs}}^{+})_{i,j,k}^{n}S_{i+1/2,j,k}\bullet+(\mathbf{A}_{\mathrm{rs}}^{+})_{i,j,k}^{n}S_{i,j+1/2,k}\bullet+(\mathbf{A}_{\mathrm{rs}}^{+})_{i,j,k}^{n}S_{i,j,k+1/2}\bullet\right.$$
$$\left.+(\mathbf{A}_{\mathrm{rs}}^{+})_{i-1,j,k}^{n}S_{i-1/2,j,k}\bullet+(\mathbf{A}_{\mathrm{rs}}^{+})_{i,j-1,k}^{n}S_{i,j-1/2,k}\bullet+(\mathbf{A}_{\mathrm{rs}}^{+})_{i,j,k-1}^{n}S_{i,j,k-1/2}\bullet]\right)\Delta\mathbf{w}_{\mathrm{rs}}^{n}$$
$$=\frac{\Delta t}{V}\mathbf{R}_{\mathrm{rs}}^{n}; \tag{44}$$

backward sweep,

$$\left(\mathbf{I}+\frac{\Delta t}{V}[(\mathbf{A}_{\mathrm{rs}}^{-})_{i,j,k}^{n}S_{i-1/2,j,k}\bullet+(\mathbf{A}_{\mathrm{rs}}^{-})_{i,j,k}^{n}S_{i,j-1/2,k}\bullet+(\mathbf{A}_{\mathrm{rs}}^{-})_{i,j,k}^{n}S_{i,j,k+1/2}\bullet\right.$$
$$\left.+(\mathbf{A}_{\mathrm{rs}}^{-})_{i+1,j,k}^{n}S_{i+1/2,j,k}\bullet+(\mathbf{A}_{\mathrm{rs}}^{-})_{i,j+1,k}^{n}S_{i,j+1/2,k}\bullet+(\mathbf{A}_{\mathrm{rs}}^{-})_{i,j,k+1}^{n}S_{i,j,k+1/2}\bullet]\right)\Delta\mathbf{q}_{\mathrm{rs}}^{n}$$
$$=\Delta\mathbf{w}_{\mathrm{rs}}^{n}; \tag{45}$$

update solution,

$$\mathbf{q}_{\mathrm{rs}}^{n+1}=\mathbf{q}_{\mathrm{rs}}^{n}+\Delta\mathbf{q}_{\mathrm{rs}}^{n}. \tag{46}$$

4.1. Gradient terms

The diffusive fluxes $\mathbf{G}_{\mathrm{v}}$ and $\mathbf{D}_{\mathrm{rs}}$ contain gradient (transport) terms that have to be evaluated on the surfaces. Since solution variables are located at cell centres, a method must be devised to properly handle these terms. The procedure used here is based on the work of Vinokur[45] in which the gradient of a scalar is evaluated based on the conservative definition

$$\frac{\partial\phi}{\partial x_k}=\frac{1}{V^*}\int_{V^*}\frac{\partial\phi}{\partial x_k}\,\mathrm{d}V^*. \tag{47}$$

A superscript asterisk on a variable implies reference to a secondary cell. Thus V^* refers to the volume of a secondary cell whose centroid coincides with the centroid of the surface where the gradient is to be evaluated. The representation of the secondary cell is shown in Figure 2. In this figure, *A*1–*B*1–*B*3–*A*3–*A*1 is the top surface of the left main cell, *A*3–*B*3–*B*5–*A*5–*A*3 is the top surface of the right main cell and *A*2–*B*2–*B*4–*A*4–*A*2 is the top surface of the secondary cell whose centroid is coincident with the centroid of the connecting surface with edge *A*3–*B*3.

Appling the divergence theorem to equation (47) gives

$$\frac{\partial\phi}{\partial x_k}=\frac{1}{V^*}\int_{S^*}n_k\phi\,\mathrm{d}S^*. \tag{48}$$

The integral in equation (48) can be evaluated as

$$V^*\frac{\partial\phi}{\partial x_k}=(\phi n_k S^*)_{i+1,j,k}+(\phi n_k S^*)_{i,j,k}+(\phi n_k S^*)_{i+1/2,j+1/2,k}$$
$$+(\phi n_k S^*)_{i+1/2,j-1/2,k}+(\phi n_k S^*)_{i+1/2,j,k+1/2}+(\phi n_k S^*)_{i+1,j,k-1/2}. \tag{49}$$

Here the indices $i, i+\frac{1}{2}, i+1$, etc. are unique and apply to both primary and secondary cells. Thus, while $i, i+1, i+2$, etc. are the centroids of primary cells, they are the surfaces of secondary cells. Now the ϕs, surface areas and volumes of the secondary cells must be estimated with due regard to conservation. Since true conservation is required only on the original cells, suitable averages can be

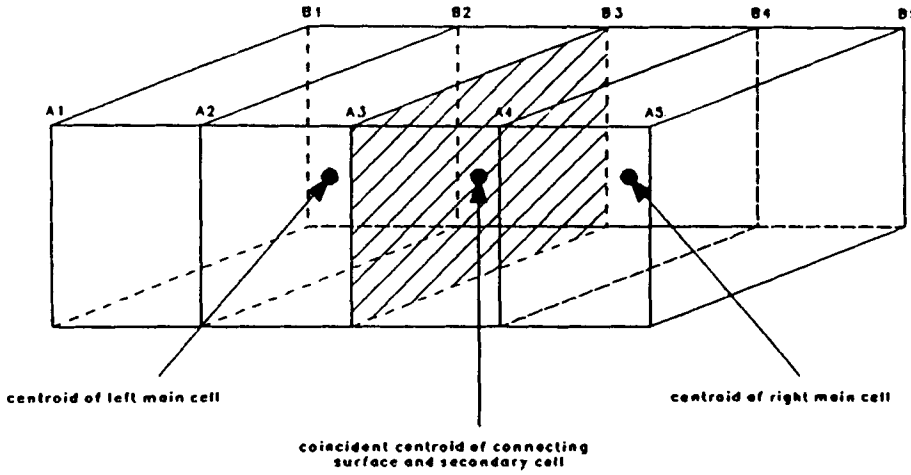

Figure 2. Schematic of the secondary cells used for the evaluation of the gradient terms. Here a secondary cell is formed as the union of the right half of the cell on the left and the left half of the cell on the right

taken for these quantities in the secondary cell. For example, the volume of the secondary cell whose centroid corresponds to the centroid of the surface $(i+\frac{1}{2},j,k)$ is evaluated by

$$V^* = \frac{V_{i,j,k} + V_{i+1,j,k}}{2}. \tag{50}$$

Similarly, the area of the surface $i+1,j,k$ of the secondary cell is

$$S^*_{i+1,j,k} = \frac{S_{i+1/2,j,k} + S_{i+3/2,j,k}}{2}. \tag{51}$$

The value of ϕ at the surface $i+1,j,k$ of the secondary cell is obtained from the conserved variables which already reside there. However, when ϕ is to be evaluated at $i+1/2,j+\frac{1}{2},k$, for example, it is found from[45]

$$\phi^*_{i+1/2,j+1/2,k} = \tfrac{1}{4}(\phi_{i,j+1,k} + \phi_{i+1,j+1,k} + \phi_{i,j,k} + \phi_{i+1,j,k}). \tag{52}$$

When the divergence of a vector is needed, ϕ is replaced by ϕ_k in the above equations and the dot product is used. When the term $\partial\phi_k/\partial x_i$ is to be evaluated in the ith momentum equation, the normal n_k is replaced by the appropriate n_x, n_y, or n_z and ϕ is replaced by ϕ_k.

4.2. Implementation of boundary conditions

Our implementation of boundary conditions is described briefly in this subsection. The physical boundaries of the domain coincide with control volume surfaces. Specified (Dirichlet) quantities are stored at the centroids of surfaces, ready for use in the evaluation of surface terms.

For Neumann conditions on a boundary the normal derivative of the variable is prescribed in the form

$$\left(\frac{\partial\phi}{\partial n}\right)_{\text{wall}} = f(\mathbf{x}, t).$$

A second-order, one-sided difference method similar to that in Reference 46 is used. This procedure will be illustrated with Figure 3.

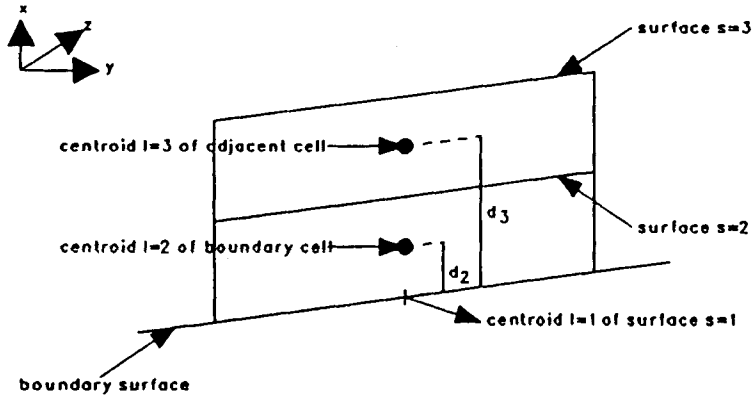

Figure 3. Schematic of the implementation of Neumann boundary conditions at a physical boundary. Here two cells cross-stream from the boundary are shown, with centroids located at d_2 and d_3 respectively from the boundary surface

A Taylor series expansion of a variable ϕ about the surface centroid, denoted by point $l = 1$, gives

$$\phi_{l=2} = \phi_{l=1} + \left(\frac{\partial \phi}{\partial n}\right)_{l=1} d_2 + \frac{(\partial^2 \phi / \partial n^2)_{l=1} d_2^2}{2} + O(d_2^3), \tag{53}$$

$$\phi_{l=3} = \phi_{l=1} + \left(\frac{\partial \phi}{\partial n}\right)_{l=1} d_3 + \frac{(\partial^2 \phi / \partial n^2)_{l=1} d_3^2}{2} + O(d_3^3). \tag{54}$$

Here d_2 and d_3 are the 'near-normal' distances from the wall to the cell centroids at $l = 2$ and 3 respectively. These distances are estimated as

$$d_2 = \frac{V_2}{S_1 + S_2}, \tag{55}$$

$$d_3 = 2d_2 + \frac{V_3}{S_2 + S_3}, \tag{56}$$

where V_2 is the volume of the boundary cell and V_3 is the volume of the cell adjacent to the boundary cell and having surface S_2 in common; S_1, S_2 and S_3 are the areas of the boundary surface of the cell, of the surface connecting the adjacent cell to the boundary cell and of the opposite surface to the connecting surface respectively.

From equations (53) and (54) the variables at the centroid of the boundary surface of the boundary cell can be evaluated as

$$\phi_1 = \frac{(\partial \phi / \partial n)_{l=1} (d_3 d_2^2 - d_2 d_3^2) + d_3^2 \phi_2 - d_2^2 \phi_3}{d_3^2 - d_2^2}. \tag{57}$$

5. SAMPLE CALCULATIONS

5.1. Shock tube

The shock tube problem, which is a widely used benchmark, is employed to validate the inviscid version of our code. In the present work the test is done for the three co-ordinate directions, one at a time.

In the initial state a diaphragm located at x_0 separates a perfect gas into two sections with different densities and static pressures (Figure 4). To the left of the diaphragm, the driver section, we have $p = 1, \rho = 1$ and $u = 0$. To the right, the driven section, $p = 0{\cdot}1$, $\rho = 0{\cdot}125$ and $u = 0$. These initial conditions were taken from Reference 47. At time $t > 0$ the diaphragm is broken, allowing a rarefaction wave to move into the high-pressure region and a shock wave followed by a contact discontinuity to propagate into the low-pressure region.

The boundary conditions for this problem are as follows. On the left, $p = 1, \rho = 1$ and $u = 0$. At the right, $p = 0{\cdot}1$, $\rho = 0{\cdot}125$ and $u = 0$.

A uniform mesh consisting of 100 elements, corresponding to an element volume $V = 0{\cdot}01$ was chosen to match that in References 8, 47 and 48. Further, the ratio $\Delta t/V = 0{\cdot}4$, Sod's standard[47] for the comparison studies, and a CFL number of 0·95 were used. Convergence to steady state is obtained in approximately 2000 time steps.

5.1.1. Results. Figure 5 shows the results of pressure, density and velocity as a function of distance (x) along the shock tube. Excellent agreement is found in comparison with the results obtained by Steger and Warming[8] and Roe.[48] as the results lie on the same curves. The superiority of our scheme is evident when the results here are compared with the various finite difference schemes used by Sod.[47] For example, both the MacCormack and Lax–Wendroff schemes produce oscillations behind the shock and the transition of the shock occupies about 10 cells. In our scheme the shock occupies roughly three to five cells with no oscillations. The efficiency of the present method was improved by freezing the evaluation of the Jacobian matrices every 10 time steps.

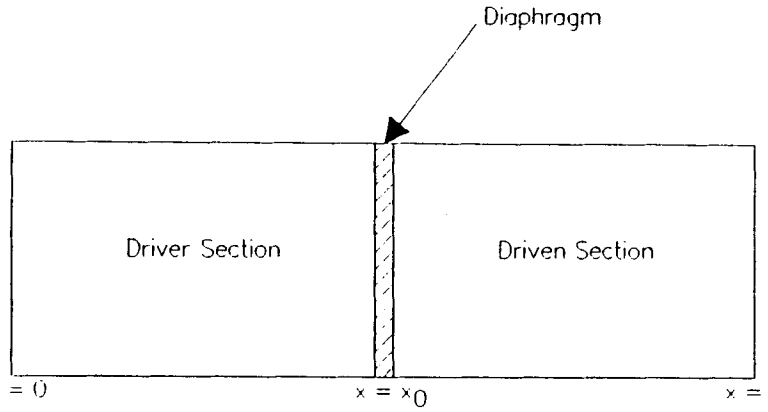

Initial Conditions

Driver Section	Driven Section
$\rho = 1$	$\rho = .125$
u = 0	u = 0
p = 1	p = .1

Figure 4. Set-up of the benchmark shock tube problem of Sod[47] showing the initial conditions. The boundary conditions at the left and right of the tube are given in the text

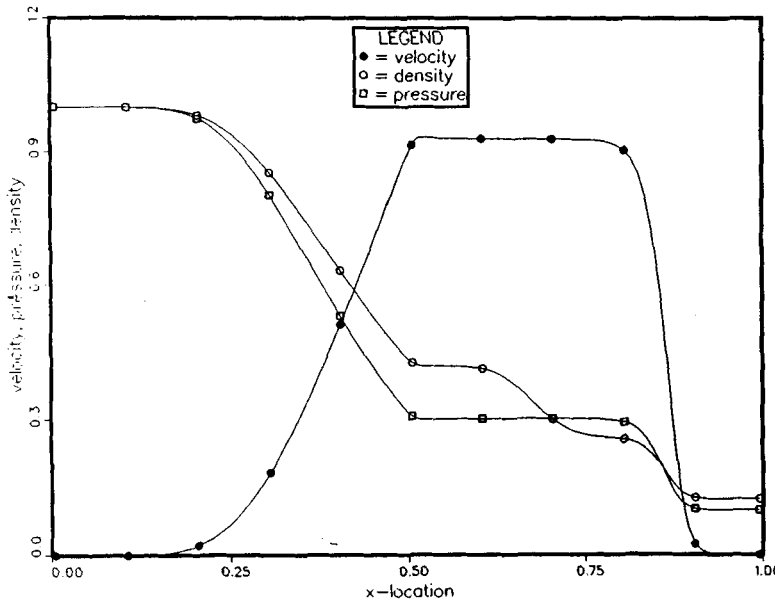

Figure 5. Results for the shock tube problem. Our calculations agree perfectly with the best results of Sod,[47] as the points from our calculation and the other results in Reference 47 lie on the same curve. Excellent agreement is also found with the results of Roe[46] and Steger and Warming[8]

5.1.2. Computing performance. On an IBM RS/6000 Model 530 the speed of computation is 0·00045 s per time step per cell. It should be realized, however, that some of the calculations, which are three-dimensional, are redundant and a lower CPU time will be expected for a truly one-dimensional version of our code.

5.2. Carter's problem

The numerical solution of laminar supersonic flow over a flate plate was chosen to validate our programme for the Navier–Stokes equations. Carter's problem[49] consists of a Mach 3 ($M_\infty = 3$) shocked flow passing over an infinitely thin plate at zero angle of attack (Figure 6). The problem is two-dimensional. The Reynolds number Re_∞ based on the plate length is 1000. The non-dimensional x-co-ordinate (streamwise) stretches from 0 to 1·4, although the plate occupies only a distance of 1·2 downstream. The non-dimensional y-co-ordinated (cross-stream) stretches from 0 to 0·8. All lengths are non-dimensionalized by the dimensional length of the plate.

The Sutherland viscosity law is used in the non-dimensional form

$$\mu = \frac{4 \cdot 1745 T^{1 \cdot 5}}{2 \cdot 769 T + 1 \cdot 406}. \tag{58}$$

The boundary conditions are

(i) *upstream* $(x = 0, y)$ $\rho = 1,$ $\rho u_1 = 1,$ $\rho u_2 = 0,$ $T = 1,$

$$\rho E = \frac{\rho T}{\gamma(\gamma - 1) M_\infty^2} + \frac{\rho u_1^2}{2}$$

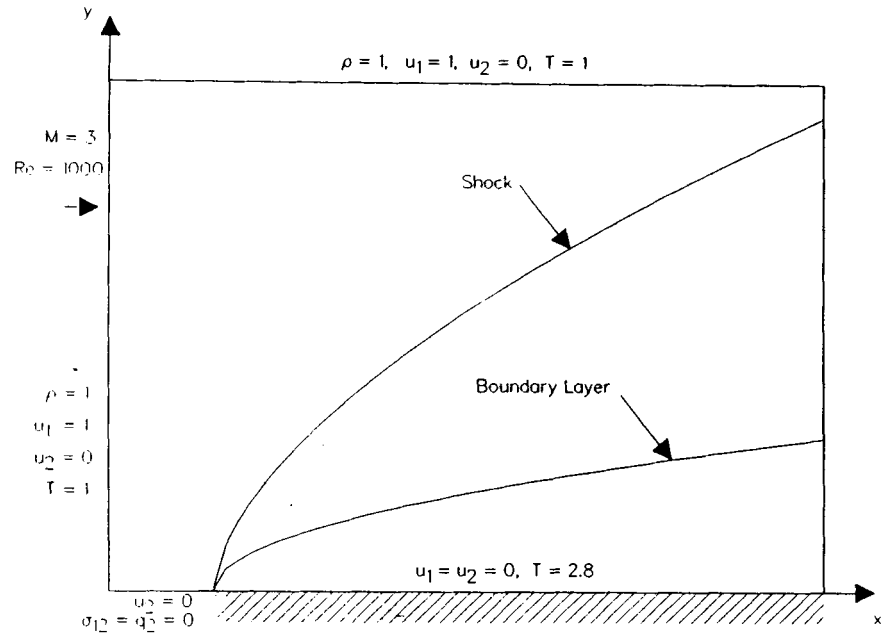

Figure 6. Schematic description of the Carter problem. This is a laminar supersonic ($M_\infty = 3$) flow on a flat plate

(ii) *symmetry condition* $(0 < x < 0{\cdot}2,\ y = 0)$

$$\sigma_{12} = 0, \quad q_2 = 0, \quad \rho u_2 = 0, \quad \frac{\partial \rho}{\partial y} = 0, \qquad \frac{\partial(\rho E)}{\partial y} = 0$$

(iii) *plate* $(0{\cdot}2 \leq x \leq 1{\cdot}4,\ y = 0)$

$$\rho u_1 = 0,\ \rho u_2 = 0,\ \frac{\partial \rho}{\partial y} = 0, \qquad T = 2{\cdot}8, \qquad \frac{\partial(\rho E)}{\partial n} = 0$$

(iv) *top boundary* $(x,\ y = 0{\cdot}8)$

$$\rho = 1, \qquad \rho u_1 = 1, \qquad \rho u_2 = 0, \qquad T = 1,$$

$$\rho E = \frac{\rho T}{\gamma(\gamma - 1)M_\infty^2} + \frac{\rho u_1^2}{2}.$$

Finally, the boundary conditions applied downstream ($x = 1{\cdot}4$, y) are found by setting the gradients of the conserved variables to zero along the surface. That is, the variables at the downstream surface are extrapolated using the second-order, one-sided gradient procedure presented earlier in this paper. For all variables, initial conditions are set to the upstream conditions.

Solutions were obtained for two topologically similar meshes, one consisting of 105 elements in the x-direction and 66 elements in the y-direction. The other mesh (mesh 2) has the same number of elements in the x-direction but 91 elements in the y-direction (Figure 7). Both meshes have the closest centroid located at distance of 0·0025 away from the wall. Results for both meshes were indistinguishable. A non-dimensional time step of 0·001 was used for time-accurate calculations with both meshes, resulting in a CFL number of 0·8 for both meshes. The equations are marched to steady state and convergence requires approximately 5000 time steps for both meshes.

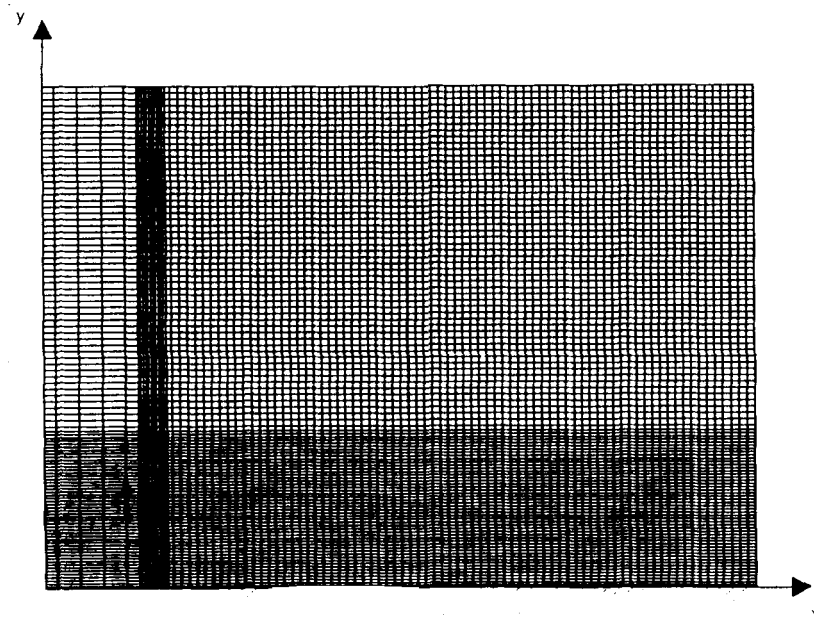

Figure 7. Computational grid (mesh 2) for the Carter problem. There are 105 cells streamwise and 91 cells cross-stream

5.2.1. Results. Comparisons were made between contour maps from our calculations for T, Mach number, ρ and p and those reported from the finite element calculations of Shakib.[49] A more quantitative comparison is shown in Figure 8 for the computed surface pressure coefficient, defined as

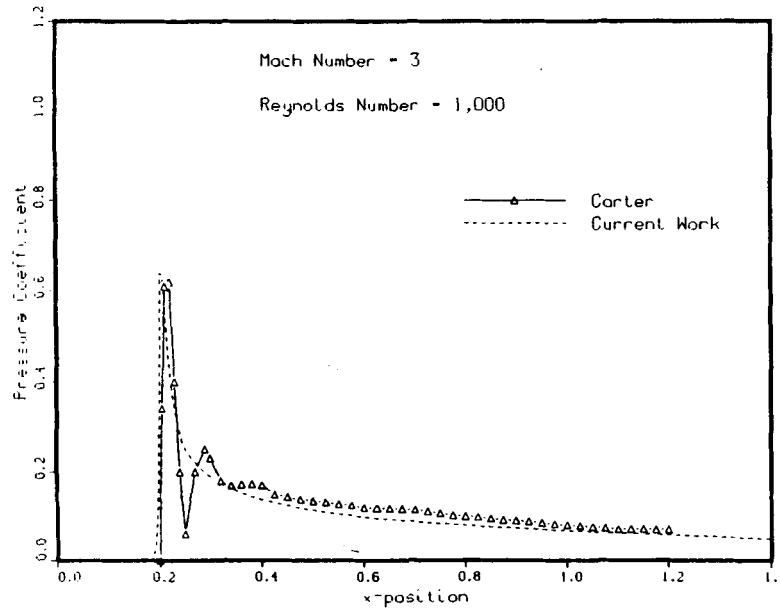

Figure 8. Pressure coefficient from our calculations and from Carter's calculations

$$C_p = \frac{p - p_\infty}{\frac{1}{2}\rho_\infty u_{1,\infty}^2}, \tag{59}$$

for mesh 2. This figure also contains the value of C_p found from Carter's experiment, which were taken from Reference 49. Close agreement is evident except in a small region just after the leading edge, where oscillations are observed in Carter's results. It seems that the calculations of Carter are in error in this region, since many studies, exemplified by those of Shakib[49] and Brueckner *et al.*[50] using various procedures have not been able to reproduce these oscillations.

5.2.2. Computing performance. The speed of computation for the Carter problem is 0·0011 s per time step per cell on the IBM RS/6000 Model 530. If we compare this performance with that for the shock tube problem, we find that it takes nearly 25% more CPU time when calculating Navier–Stokes solutions with an explicit treatment of the viscous terms. Again it should be noted here that the code is running as though calculations were taking place for three dimensions, so the CPU time should be viewed accordingly.

5.3. Zero-pressure-gradient supersonic turbulent boundary layer

Compressible turbulence in a zero-pressure-gradient boundary layer was one of the problems chosen to validate our code for the turbulence calculations. We compare our results with the measurements by Spina and Smits,[51] who carried out a fundamental study of this problem. The Reynolds number per unit length, Re/m is $6{\cdot}5 \times 10^7$ and $M_\infty = 2{\cdot}87$.

The computational domain extends 0·5 m along x and 0·018 m along y. The dynamic viscosity is assumed to depend only on temperature and to obey the Sutherland law.[33]

The boundary conditions for this problem are shown in Figure 9. Downstream ($x = 0{\cdot}5$, y) the normal gradients of the conserved variables are set to zero. Similar conditions are used at the top of the domain ($x, y = 0{\cdot}018$). Initial conditions were obtained by generalizing the procedure of Gerolymos[52] with an initial external turbulence intensity of 0·1%. The mesh used for the results shown in this paper (Figure 10) consists of 170 cells in the x-direction and 70 non-uniform cells in the y-direction. The centroid of the first cell along the plate is located at $y^+ \approx 0{\cdot}35$; the mesh has 25 cells in $y^+ \leq 50$, a maximum aspect ratio of approximately 2778 for any cell and extends for approximately three boundary layers in the transverse direction. A time step size of 2×10^{-9} s is used for the calculations. (Note that the Reynolds number is of the order of 10^7.) The equations are marched in time and convergence was obtained at approximately 7500 time steps.

5.3.1. Results. First the results at locations $x = 0{\cdot}3$ and 0·5 m along the plate were compared and found to be essentially the same. For the purpose of comparison with the experimental measurements we assume $\bar{\phi} = \tilde{\phi}$ and $\bar{\phi}' \approx 0$. Results are presented for $x = 0{\cdot}5$ m. These results are non-dimensionalized to compare them with the experimental results of Spina and Smits.[51] The compared results are shown in Figures 11–13 respectively for the mean velocity, the Mach number and the profile of log-law velocity u^+ after van Driest transformation. Excellent agreement between the present work and experimental measurements is apparent. The broken line in Figure 13 represents the familiar analytical log-law results.

5.4. Supersonic turbulent flow on a concave wall

As a final demonstration of the potential usefulness of the schemes presented in this paper, we will discuss the calculation of a supersonic turbulent boundary layer experiencing the combined effects of an adverse pressure gradient, bulk compression and concave streamline curvature.[53,54] These effects

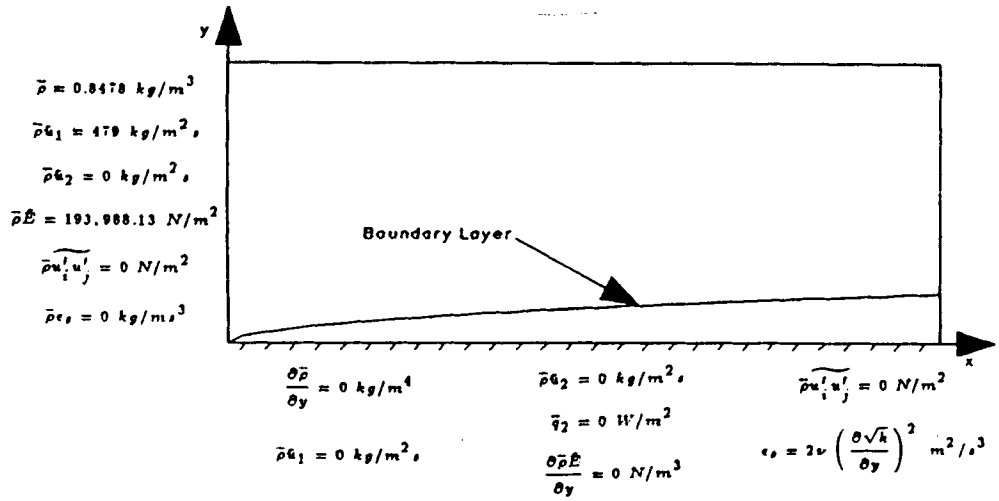

Figure 9. Model for the supersonic turbulent boundary layer problem of Spina and Smits[51] showing the boundary conditions

result from flows over short regions of concave surface curvature. The upstream of the ramp consists of a Mach 2·87 boundary layer of thickness $\delta = 0{\cdot}025$ m. The total pressure is $6{\cdot}9 \times 10^5$ N m^{-2} and the Reynolds number is $6{\cdot}3 \times 10^7$ m^{-1}. The strong adverse pressure gradient case in which the boundary layer thickness-to-curvature ratio (δ/R_c) is 0·1 is calculated. More details of the flow conditions are available in References 53 and 54.

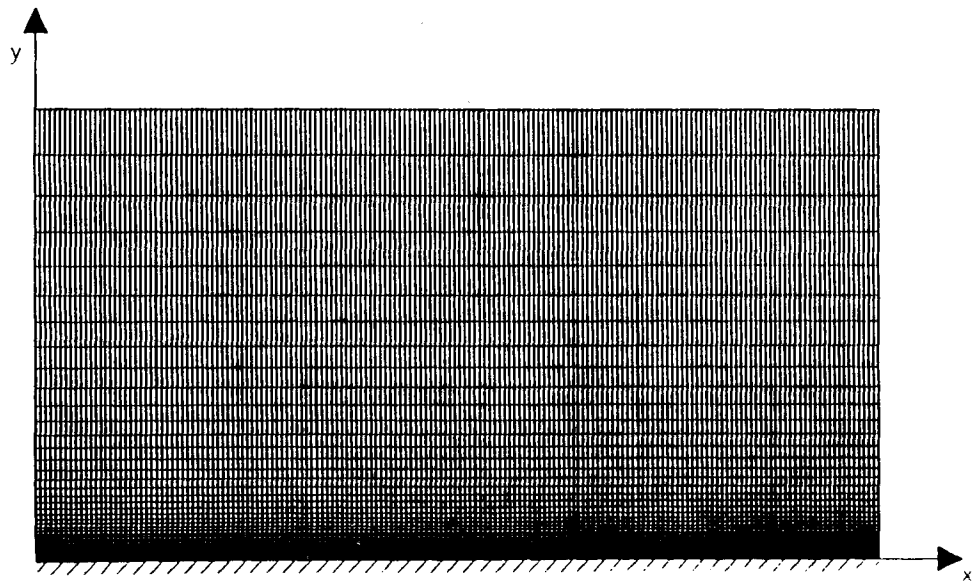

Figure 10. Computational grid used for the simulation of the supersonic turbulent boundary layer problem of Spina and Smits.[51] There are 170 uniform cells streamwise and 70 non-uniform cells cross-stream. The largest cell aspect ratio is 2778, which occurs in cells adjacent to the boundary

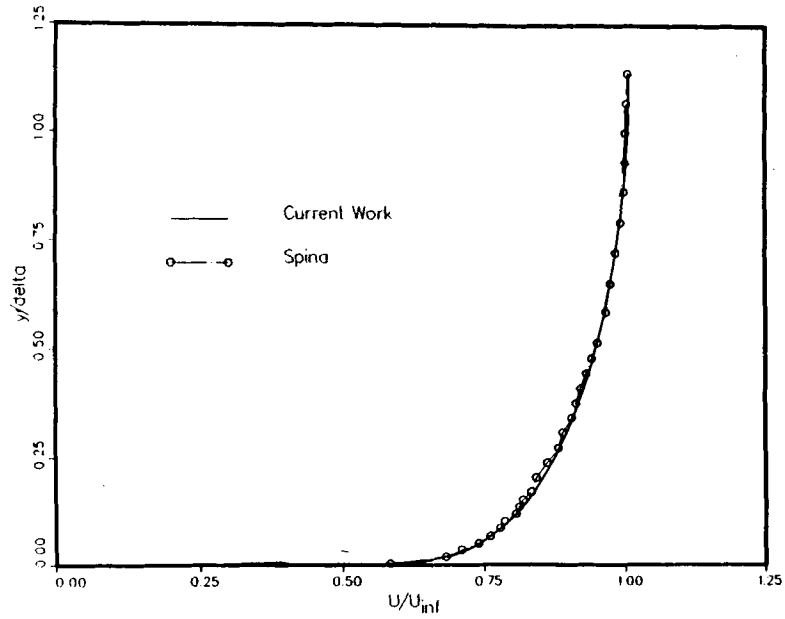

Figure 11. Comparison of the profile of mean velocity $\tilde{u}_1/U_\infty$ in our calculations and in the measurements of Spina and Smits[51]

Sample computed results are contained in Figures 14 and 15, where we show the wall pressure p_w/p_∞ and the skin friction C_f respectively as functions of x/δ. The experimental measurements from References 53 and 54 are also shown in these figures. Good agreement is evident.

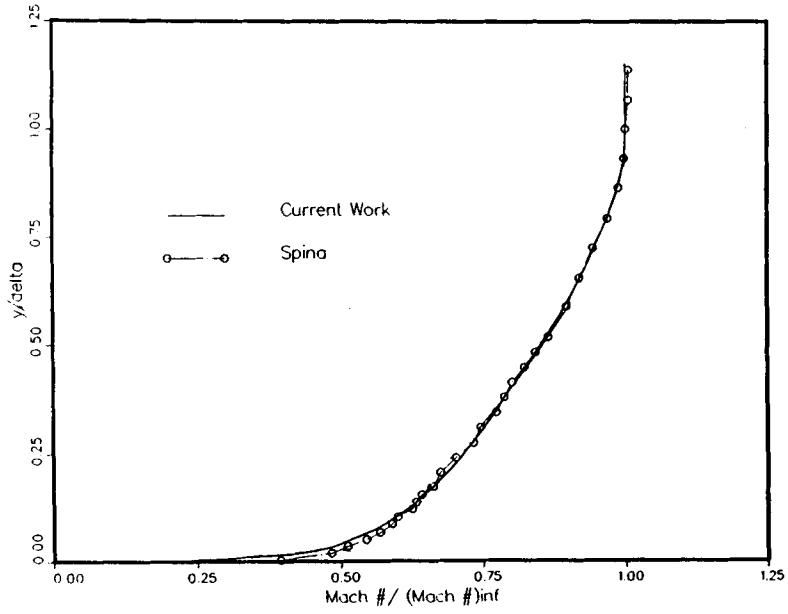

Figure 12. Comparison of the profile of mean Mach number M/M_∞ in our calculations and in the measurements of Spina and Smits[51]

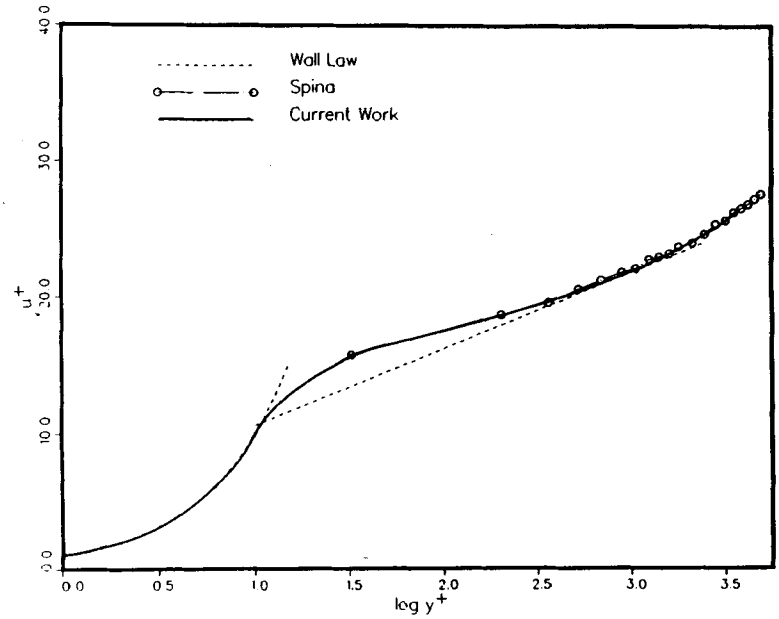

Figure 13. Profile of log-law velocity u^+ after van Driest transformation for supersonic turbulent boundary layer flow with zero pressure gradient

5.4.1. Computing performance. The speed of computation of turbulent flows using second moments is 0·00394 s per time step per cell on the IBM RS/6000 Model 530. When compared with the performance for Carter's problem, it takes approximately four times more CPU time for the solution of turbulent flow calculations using second-moment closures.

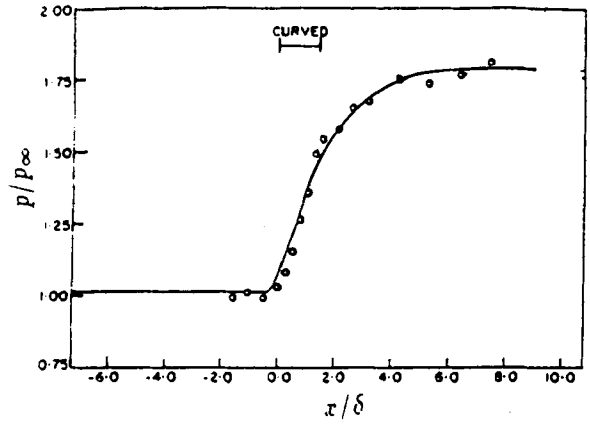

Figure 14. Wall pressure as a function of x for supersonic turbulent flow over a concave wall. The symbols are experimental measurements while the full curve represents computed results

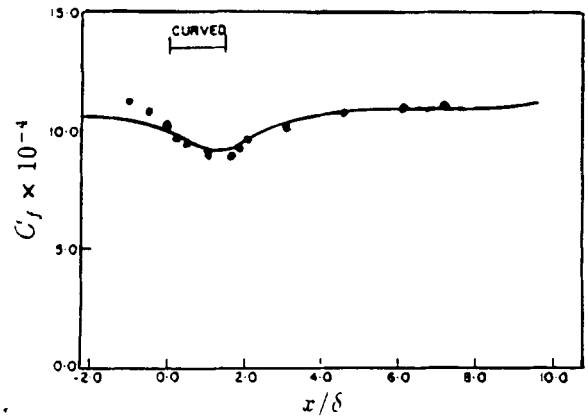

Figure 15. Skin friction as a function of x for supersonic turbulent flow over a concave wall. The symbols are experimental measurements while the full curve represents computed results

6. CONCLUSIONS

Combining FVS and FDS and treating the viscosity terms explicitly produces very accurate calculations for both the Euler and the full Navier–Stokes equations. We have extended this baseline scheme, which is based on laminar or eddy viscosity flows, to include the equations for the six components of Reynolds stress and an additional equation for turbulence dissipation. Comparisons of our turbulence calculations with recent experimental measurements of supersonic turbulent boundary layers by Spina and Smits[51] show very good agreement for most of the quantities compared. We also calculated a supersonic turbulent boundary layer experiencing the combined effects of an adverse pressure gradient, bulk compression and concave streamline curvature. The agreement with the results of Degani and Smits[54] and Jayaram *et al.*[55] is excellent. The speeds of computation (in seconds per time step per cell) on an IBM RS/6000 Model 530 workstation for the shock tube problem, Carter's supersonic laminar boundary layer problem and the supersonic turbulent boundary layer with second-moment closures are 0·00045, 0·0011 and 0·00394 respectively. However, in all cases the code is running as if calculations were taking place for a three-dimensional problem, so the CPU times should be viewed accordingly. Based on the agreement of the computed results with experimental data, it would seem that the schemes presented in this paper are potentially quite useful.

ACKNOWLEDGEMENT

We wish to express our sincere appreciation to Professor Edward E. O'Brien for fruitful discussions on the more physical aspects of this investigation.

REFERENCES

1. C. G. Speziale, 'Analytical methods for the development of Reynolds-stress closures in turbulence, *Ann. Rev. Fluid Mech.*, **23**, 107–157 (1991).
2. B. S. Baldwin and H. Lomax 'Thin-layer approximation and algegraic model for separated turbulent flows', *AIAA Paper 78-257*, 1978.
3. J. Lee, D. B. Taulbee and M. S. Holden, 'Study of turbulence on supersonic compression surfaces using Reynolds stress model', *AIAA J.*, **30**, 1738–1746 (1992).

4. P. L. Roe, 'The use of the Riemann problem in finite-difference schemes', *Lecture Notes in Physics*, **141**, 354–359 (1980).
5. A. Harten and P. D. Lax, 'A random choice finite difference scheme for hyperbolic conservation laws', *SIAM J. Numer. Anal.*, **18**, 289–315 (1981).
6. V. V. Rusanov, *Zh. Vych. Mat. Mat. Fiz*, **1**, 267–279 (1961).
7. B. van Leer, 'Flux-vector splitting for the Euler equations', *Lecture Notes in Physics*, **170**, 507–512 (1982).
8. J. L. Steger and R. F. Warming, 'Flux vector splitting of the inviscid gasdynamic equations with application to finite-difference methods', *J. Comput. Phys.*, **40**, 263–293 (1981).
9. A. Jameson, W. Schmidt and E. Turkel, 'Numerical solutions of the Euler equations by finite volume methods using Runge–Kutta time-stepping schemes', *AIAA Paper 81-1259*, 1991.
10. R. W. MacCormack, 'The Effect of viscosity in hypervelocity impact cratering', *AIAA Paper 69-354*, 1969.
11. B. van Leer, J. L. Thomas, P. L. Roe and R. W. Newsome, 'A comparison of numerical flux formulas for the Euler and Navier–Stokes equation', *AIAA Paper 87-1104-CP*, 1987.
12. J. J. Quirk, 'A contribution to the great Riemann solver debate', *ICASE Report 92-64*, 1992.
13. L. B. Simpson and D. L. Whitfield, 'Flux-difference split algorithm for unsteady thin-layer Navier–Stokes equations', *AIAA J.*, **30**, 914–922 (1992).
14. B. van Leer, 'Progress in multidimensional upwind differencing', *ICASE Report 92-43*, 1992.
15. R. W. MacCormack, 'On the development of efficient algorithm for three-dimensional fluid flow', in T. E. Tezduyer and T. J. R. Hughes (eds), *Recent Developments in Computational Fluid Dynamics*, AMD Vol. 95, 19XX, pp. 117–137.
16. D. S. Chaussee and T. H. Pulliam, 'Two-dimensional inlet simulation using a diagonal implicit algorithm', *AIAA J.*, **19**, 153–159 (1981).
17. M. Jayaram and A. Jameson 'Multigrid solution of the Navier–Stokes equations for the flow over wings', *AIAA Paper 88-705*, 1988.
18. J. W. Yokota, D. A. Caughey and R. V. Chima, 'The diagonally-inverted LU implicit multigrid scheme', *Proc. First Nat. Fluid Dynamics Congr.*, Washington, DC, July 1988, Part 1, AIAA, New York, 1988, pp. 104–111.
19. D. A. Caughey, 'Diagonal implicit multigrid algorithm for Euler equations', *AIAA J.*, **26**, 841–851 (1988).
20. J. W. Yokota, 'Diagonally inverted lower–upper factored multigrid scheme for the three-dimensional Navier–Stokes equations', *AISS J.*, **28**, 1642–1649 (1990).
21. Y. Yadlin and D. A. Caughey, 'Block multigrid implicit solution of the Euler equations of compressible fluid flow', *AIAA J.*, **29**, 712–719 (1991).
22. T. L. Tysinger and D. A. Caughey, 'Multigrid ADI algorithm for the Navier–Stokes equations', *AIAA J.*, **30**, 2158–2160 (1992).
23. Y. Yadlin and D. A. Caughey, 'Parallel computing strategies for block multigrid implicit solution of the Euler equations', *AIAA J.*, **30**, 2032–2038 (1992).
24. M.-S. Liou and C. J. Steffen, Development of new flux-splitting schemes', *NASA Conf. Publ. 10078*, 19XX, pp. 19–28.
25. A. Harten, B. Enquist, S. Osher and S. R. Chakravarthy, 'Uniformly high order accurate essentially non-oscillatory schemes, III', *J. Comput. Phys.*, **71**, 231 (1987).
26. C.-W. Shu, G. Erlebacher, T. A. Zang, D. Whitaker and S. Osher, 'High-order ENO schemes applied to two- and three-dimensional compressible flow', *ICASE Report 91-38*, 1992.
27. S. K. Lele, 'Compact finite difference schemes with spectral-like resolution', *CTR Manuscript 107*, Stanford University, 1990.
28. K. J. Vanden and D. M. Belk, 'Numerical investigation of subsonic and supersonic axisymmetric vortical flows', *AIAA J.*, **31**, 1377–1383 (1993).
29. K. Hanjalic and B. E. Launder, 'Contribution towards a Reynolds-stress closure for low-Reynolds-number turbulence', *J. Fluid Mech.*, **74**, 593–610 (1976).
30. R. M. C. So, Y. G. Lai, H. S. Zhang and B. C. Hwang, 'Second-order near wall turbulence closures: a review', *AIAA J.*, **29**, 1819–1835 (1991).
31. K. Hanjalic and B. E. Launder, 'A Reynolds stress model of turbulence and its application to thin shear flows', *J. Fluid Mech.*, **52**, 609–638 (1972). Also *Int. J. Heat Mass Transfer*, **15**, 301–314 (1972).
32. B. E. Launder, G. J. Reece and W. Rodi, 'Progress in the development of a Reynolds-stress turbulence closure', *J. Fluid Mech.*, **68** 537–566 (1975).
33. J. C. Intile, 'Numerical calculations of second moments of turbulence in supersonic flows', *M.S. Thesis*, State University of New York, Stony Brook, NY, 1993.
34. B. E. Launder and N. Shima, 'Second-moment closure for the near-wall sublayer: development and application', *AIAA J.*, **27**, 1319–1324 (1989).
35. A. Harten and P. D. Lax, 'A random choice finite difference scheme for hyperbolic conservation laws', *SIAM J. Numer. Anal.*, **18**, 289–315 (1981).
36. J. Lee, 'Reynolds stress model predictions of supersonic boundary layer over compression surfaces', *Ph.D. Dissertation*, State University of New York, Buffalo, NY, 1991.
37. S. Sarkar and B. Lakshmanan, 'Application of a Reynolds stress turbulence model to the compressible shear layer', *AIAA J.*, **29**, 743–749 (1991).
38. O. Zeman, 'A new model for super/hypersonic turbulent boundary layers', *AIAA Paper 93-0897*, 1993.
39. S. Sarkar, G. Erlebacher, M. Y. Hussaini and H. O. Kreiss, 'The analysis and modelling of dilational terms in compressible turbulence', *J. Fluid Mech.*, **227**, 473–493 (1991).

40. O. Zeman, 'Dilation dissipation: the concept and application in modeling compressible mixing layers', *Phys. Fluids A*, **2**, 178–188 (1990).
41. R. M. Beam and R. F. Warming, 'An implicit finite difference algorithm for hyperbolic systems in conservation law forms', *J. Comput. Phys.*, **22**, 87–110 (1976).
42. P. L. Roe, 'Approximate Riemann solvers, parameter vectors and difference schemes', *J. Comput. Phys.*, **43**, 263–293 (1981).
43. N. T. Frink, 'Upwind scheme for solving the Euler equations on unstructured meshes', *AISS J.*, **30**, 70–77 (1992).
44. A. Jameson, W. Schmidt and E. Turkel 'Numerical solutions of the Euler equations by finite volume methods using Runge–Kutta time-stepping schemes', *AIAA Paper 81-1259*, 1991.
45. M. Vinokur, 'An analysis of finite-difference and finite-volume formulations of conservation laws', *J. Comput. Phys.*, **81**, 1–51. (1989).
46. B. Gatlin, 'An implicit, upwind method for obtaining symbiotic solutions to the thin-layer Navier–Stokes equations', *Ph.D. Dissertation*, Mississippi State University, 1987.
47. G. A. Sod, 'A survery of several finite difference methods for systems of nonlinear hyperbolic conservation laws', *J. Comput. Phys.*, **27**, 1–31 (1978).
48. P. L. Roe, 'Characteristic-based schemes for the Euler equations', *Ann. Rev. Fluid Mech.*, **18**, 337–365 (1986).
49. F. Shakib, 'Finite-element anlaysis of the compressible Euler and Navier–Stokes equations', *Ph.D. Dissertation*, Stanford University, 1988.
50. D. P. Brueckner, D. W. Pepper and R. H. Chu, 'A parallel finite element algorithm for calculating three-dimensional inviscid and viscous compressible flows', *AIAA Paper 93-0340*, 1993.
51. E. F. Spina and A. J. Smits, 'Organized structures in a compressible, turbulent boundary layer', *J. Fluid Mech.*, **182**, 85–109 (1987); see also H. H. Fernholtz, P. J. Finley, J. P. Dussauge and A. J. Smits, 'A survey of measurements and measuring techniques in rapidly distorted compressible turbulent boundary layers', *AGARD 315*, 1989.
52. G. A. Gerolymos, 'Implicit multi-grid solution of the compressible Navier–Stokes equations using k–ε turbulence closure', *AIAA J.*, **28**, 1707–1717 (1990).
53. D. Degani and A. J. Smits, 'Response of a compressible, turbulent boundary layer to a short region of surface curvature', *AIAA J.*, **27**, 23–28 (1989).
54. M. Jayaram, M. W. Taylor and A. Smits, 'The response of a compressible turbulent boundary layer to short regions of concave surface curvature', *J. Fluid Mech.*, **175**, 343–362 (1987).